Deep Eddy Energy and Topographic Rossby Waves in the Gulf of Mexico

L.-Y. OEY AND H.-C. LEE

Program in Atmospheric and Oceanic Sciences, Princeton University, Princeton, New Jersey

(Manuscript received 4 June 2001, in final form 7 June 2002)

ABSTRACT

Observations suggest the hypothesis that deep eddy kinetic energy (EKE) in the Gulf of Mexico can be accounted for by topographic Rossby waves (TRWs). It is presumed that the TRWs are forced by Loop Current (LC) pulsation, Loop Current eddy (LCE) shedding, and perhaps also by LCE itself. Although the hypothesis is supported by model results, such as those presented in Oey, the existence of TRWs in the model and how they can be forced by larger-scale LC and LCEs with longer-period vacillations have not been clarified. In this paper, results from a 10-yr simulation of LC and LCEs, with double the resolution of that used by Oey, are analyzed to isolate the TRWs. It is shown that along an east-to-west band across the gulf, approximately over the 3000-m isobath, significant EKE that accounts for over one-half of the total spectrum is contained in the 20–100-day periods. Bottom energy intensification exists in this east–west band with vertical decay scales of about 600–300 m decreasing westward. The decrease agrees with the TRW solution. The band is also located within the region where TRWs can be supported by the topographic slope and stratification used in the model and where wavenumber and frequency estimates are consistent with the TRW dispersion relation. The analysis indicates significant correlation between pairs of east–west stations, over distances of approximately 400 km. Contours of lag times suggest offshore (i.e., downslope) phase propagation, and thus the east–west band indicates nearly parabathic and upslope energy propagation. Ray tracing utilizing the TRW dispersion relation and with and without (for periods >43 days) ambient deep currents shows that TRW energy paths coincide with the above east–west high-energy band. It also explains that the band is a result of TRW refraction by an escarpment (with increased topographic gradient) across the central gulf north of the 3000-m isobath, and also by deep current and its cyclonic shear, and that ray convergence results in localized EKE maxima near 91°W and 94°–95°W. Escarpment and cyclonic current shear also shorten TRW wavelengths. Westward deep currents increase TRW group speeds, by about 2–3 km day^{-1} according to the model, and this and ray confinement by current shear may impose sufficient constraints to aid in inferring deep flows. Model results and ray paths suggest that the deep EKE east of about the 91°W originates from under the LC while farther west the EKE also originates from southwestward propagating LCEs. The near-bottom current fluctuations at these source regions derive their energy from short-period (<100 days) and short-wavelength (<200 km) near-surface fluctuations that propagate around the LC during its northward extrusion phase and also around LCEs as they migrate southwestward in the model.

1. Introduction

Topographic Rossby waves (TRWs) are subinertial motions (those we are interested in this paper have periods >20 days) induced by cross-isobathic motions as fluid columns are stretched and compressed over sloping topography. Conservation of potential vorticity requires that a fluid parcel shoved over deeper (shallower) portion of the slope attains cyclonic (anticyclonic) relative vorticity, thus wave propagation with shallower water to the right in the Northern Hemisphere (see, e.g., Gill 1982). Observational evidence of TRWs over slope and rise have been documented and analyzed especially along the continental slope of the U.S. east coast (Thompson and Luyten 1976; Hogg 1981; Louis et al. 1982; Johns and Watts 1986; Pickart and Watts 1990). These TRWs appear to be generated by deep fluctuations of the Gulf Stream and warm-core rings. Pickart (1995) found, for example, that the prominent 40-day TRWs observed on the Cape Hatteras slope could be back-traced to a region around 72°W where the zonal TRW wavenumber closely matched that of eastward propagating meanders of the Gulf Stream.

Observational evidence of TRWs in the Gulf of Mexico (GOM) was first given by Hamilton (1990) through analysis of long-term current measurements below 1000-m depth made in the late 1980s. Based on deep moorings over the slope and rise around the gulf, east from Florida to the northern and western gulf, he found energy spectral peaks at 25, 45, and 100 days, within the range of periods expected for TRWs. The motions are characterized as columnar, with amplitudes decreasing with increasing height off the seabed. The waves

---

Corresponding author address: L.-Y. Oey, Program in Atmospheric and Oceanic Sciences, Princeton University, Forrestal Campus, Sayre Hall, Princeton, NJ 08544.
E-mail: lyo@princeton.edu

are transverse and rectilinear such that the principal major axis is at an angle to the general trend of the isobaths. More detailed analyses showed that these waves have wavelengths of about 110–300 km, phase velocities that were offshore and energy propagation that was westward with speeds of approximately 9 km day^{-1}.

The Loop Current (LC), with speeds that can exceed 2 m s^{-1} near the surface and O(10 cm s^{-1}) at 1000-m depths, constitutes a major forcing to flow fluctuations in the Gulf of Mexico. On time scales from weeks to years, the LC can extrude as far northward as the Alabama–Mississippi continental rise near the foot of the De Soto Canyon and can retract southward to near the Yucatan Channel (Vukovich et al. 1979). This LC pulsation is often accompanied, at periods that range from 6 to 20 months, by shedding of Loop Current eddies (LCE), which are energetic warm-core rings (similar to those found in the Gulf Stream system) with diameters that typically range from 200 to 300 km and near-surface swirling speeds that exceed 1.5 m s^{-1} (Kirwan et al. 1988; Forristall et al. 1992; Hamilton et al. 1999). In addition, through some kind of dynamical instability, or otherwise a cascade mechanism that is not yet fully understood, smaller-scale eddies (cyclones in particular) and frontal meanders are believed to be generated from the larger-scale LC and LCEs (Paluszkiewicz et al. 1983; Hamilton 1990, 1992; Hamilton et al. 2000).

Given their ubiquitous signatures, it seems logical to hypothesize that, through some mechanisms, the Loop Current and LCEs force deep-flow eddy kinetic energy (EKE) and TRWs in the gulf. While field evidence is hard to come by, (numerical) models of the gulf, forced by time-independent forcing, suggest that this might in fact be the case (e.g., Oey 1996, hereafter O96). Motivated by Hamilton's (1990) work, Oey attempted to identify TRWs from his calculation of the LC and LCEs in the gulf. Similar to what Hamilton found, the calculations yielded columnar motions for depths deeper than 1500 m at locations over the slope and rise around the gulf, along-isobath motions that intensified near the bottom, spectral peaks within the 20–100-day periods, and westward energy propagation with speeds of about 12 km day^{-1}. By nature of the steady forcing, these findings established a direct link between LC- and LCE-induced variability and bottom EKE, though they fell short of establishing what those variability might be, and of proving that the deep motions were indeed TRWs. Moreover, it is of interest to study, if TRWs do exist, what their paths are in the gulf and whether or not (and how) they can account for EKE recorded (in model and/or field experiments) at locations that seem distant from direct LC and LCE influences. In this paper, these issues will be addressed using an improved version of the primitive equation (PE) model used by Oey (see below). We will show that, in a model forced by steady transport from the Caribbean Sea and Atlantic Ocean, the deep-flow EKE over certain parts of the slope and rise in the gulf are TRWs, that these TRWs originate from regions beneath the LC and from locations coincident with the paths of propagating LCEs, and that the link between the energy of the large-scale—that is, those of the LC and LCEs—and the near-bottom energy is surface high-frequency, short-wavelength disturbances produced around the LC and LCEs.

The outline of the paper is as follows. Section 2 reviews the TRW and ray-tracing theory that will be used and discussed in later sections. Section 3 briefly describes the numerical model and explains how LC and LCEs are simulated. These serve as forcing to the TRWs. It also outlines how we conduct model–data analyses. Section 4 presents the deep-flow EKEs as they pertain to TRW motions, and combines the PE model and TRW ray-tracing model results to provide information as to TRW energy propagation velocities, ray (energy) convergence zones, and horizontal (wavelengths) and vertical scales. Section 5 discusses the sources of deep EKE, and section 6 concludes the paper.

2. Topographic Rossby waves and ray tracing

We will rely on quasigeostrophic (QG) dynamics for detecting and interpreting TRWs from the results of a PE model—the Princeton Ocean Model (POM; Mellor 1993). For typical $N/f \approx 10$ and maximum slope gradients $|\nabla h| < \approx 0.05$ used in the model, where ∇ is the horizontal gradient operator; h = water depth; N = Brunt–Väisälä frequency, henceforth assumed constant; and f = Coriolis parameter, it can be shown that the QG dispersion is valid for wave periods ≥20 days (appendix A). We will therefore focus solely on waves with periods >20 days. The QG dispersion relation is given by two coupled equations (Pedlosky 1979; Pickart 1995):

$$\mu = N(K^2 + \beta k/\sigma)^{1/2}/f \quad \text{and} \tag{1a}$$

$$\sigma/f = (\mathbf{K} \times \nabla h)_z N^2/[\mu f^2 \tanh(\mu h)], \tag{1b}$$

where $\mathbf{K} = (k, l)$ = horizontal (x–y plane) wavenumber vector; $K^2 = k^2 + l^2$; σ is the frequency; $(\mathbf{K} \times \nabla h)_z = (kh_y - lh_x)$, the z component of the vector $\mathbf{K} \times \nabla h$; $\beta = \partial f/\partial y$, the planetary beta; and the ocean is assumed to be unbounded with a rigid lid at $z = 0$. When topographic slope dominates, $\beta_{\text{Topo}} = f|\nabla h|/h \gg \beta$, and the β term can be dropped. Then μ can only be real, and it becomes the inverse vertical trapping scale of the wave. Equation (1) then gives

$$\sigma \tanh(NhK/|f|)/N = \text{sgn}(f)(\mathbf{n}_\mathbf{K} \times \nabla h)_z, \tag{2}$$

where $\mathbf{n}_\mathbf{K} = \mathbf{K}/K$ is the wavenumber unit vector, sgn(f) = sign of f, and subscript z denotes the z component of the vector $\mathbf{n}_\mathbf{K} \times \nabla h$. Without loss of generality, σ can be taken to be greater than 0, so that $(\mathbf{n}_\mathbf{K} \times \nabla h)_z$ must have the same sign as sgn(f). Thus the phase propagation direction must lie to the right (left) of the direction of increasing water depth in the Northern (Southern) Hemisphere. In other words, the wavenum-

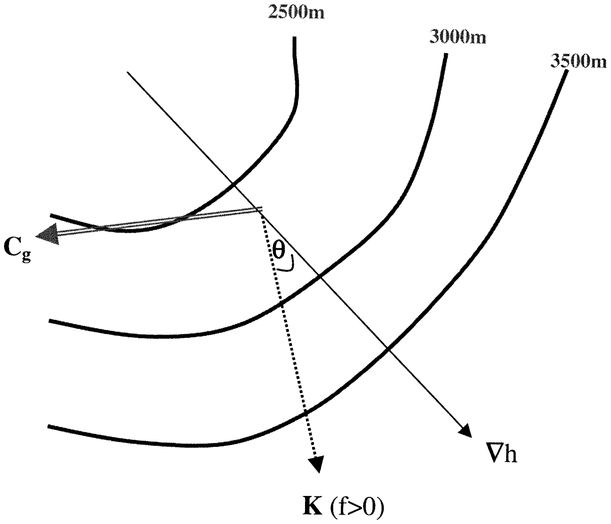

FIG. 1. A schematic that describes the relations between three vectors: the gradient of water depth ∇h, wavenumber vector $\mathbf{K}$, and the group velocity $\mathbf{C}_g$ in the Northern Hemisphere and when $NhK/f \approx O(1)$ or larger (see text). The θ is the clockwise angle that $\mathbf{K}$ makes with ∇h. The $\mathbf{C}_g$ is very nearly perpendicular to $\mathbf{K}$. Moreover, $\mathbf{C}_g \times \mathbf{K} \propto \cos(\theta)$, so that it is positive (negative) and $\mathbf{C}_g$ points upslope (downslope) when $\mathbf{K}$ points downslope (upslope) when $0 < \theta < \pi/2$ ($\pi/2 < \theta < \pi$). The figure shows the case $0 < \theta < \pi/2$.

ber vector makes a *clockwise* (*anticlockwise*) angle θ with respect to the direction of steepest topographic decent (i.e., with $\nabla h/|\nabla h|$). For $NhK/|f| \approx O(1)$ or larger (which typically requires wavelengths <200 km), $\tanh(NhK/|f|) \approx 1$, or at most a weak function of $NhK/|f|$, and (2) shows that the frequency σ is independent of the magnitude of the wavenumber and depends only on the angle that the wavenumber vector makes with the x or y axis. It follows then that the component in the direction of $\mathbf{K}$ of the rate of change of frequency in the wavenumber space, $\mathbf{n}_\mathbf{K} \cdot \nabla_\mathbf{K}\sigma$, where $\nabla_\mathbf{K} = (\partial/\partial k, \partial/\partial l)$, must be zero, since this direction is by definition fixed and σ itself depends on it only and not on the magnitude K. Thus, the wavenumber vector and group velocity $\mathbf{C}_g$ ($=\nabla_\mathbf{K}\sigma$) must be perpendicular to each other. Moreover, (1b) [with $\tanh(NhK/|f|) \approx 1$] gives

$$\mathbf{C}_g = N\mathbf{n}_\mathbf{K} \cdot \nabla h\,(l, -k)/K^2, \tag{3}$$

so that $\mathbf{C}_g \times \mathbf{K} = N\mathbf{n}_\mathbf{K} \cdot \nabla h = N|\nabla h| \cos(\theta)$. Thus $\mathbf{C}_g$ is directed clockwise (upslope) with respect to $\mathbf{K}$ when the latter points downslope, $0 < \theta < \pi/2$, and anticlockwise (downslope) when $\mathbf{K}$ points upslope, $\pi/2 < \theta < \pi$ (Fig. 1).

Ray tracing

Knowing the dispersion relation (1), we will use the ray-tracing technique [please see, e.g., Lighthill 1978, who gives a succinct account based on the Wentzel–Kramer–Brillouin (WKB)] to follow the path of TRW energy produced in the PE model simulation. Path (or ray) calculations will aid in locating possible sources of TRW energy in the gulf. The method assumes that a group of TRWs travels with slowly varying amplitude and is locally nearly sinusoidal with a phase $\alpha(x_i, t)$, so that

$$\partial\alpha/\partial x_i = -k_i, \tag{4a}$$

$$\partial\alpha/\partial t = \sigma(k_i, E_n), \qquad i = 1, 2, \tag{4b}$$

where the suffix i is used to denote east–west and north–south coordinates (x_1, x_2) and wavenumber vector (k_1, k_2), and repeated suffix on i or j (see below) means summation from 1 to 2. The E_n denotes any of the environmental parameters N, h, h_x, and h_y, and repeated suffix on n means summation from 1 to 4. One can differentiate (4b) with respect to x_i and use (4a):

$$\partial k_i/\partial t + C_{gj}(\partial k_i/\partial x_j) = -(\partial\sigma/\partial E_n)(\partial E_n/\partial x_i), \quad \text{or} \tag{5a}$$

$$dk_i/dt = -\partial\sigma/\partial x_i, \tag{5b}$$

where $C_{gj} = \partial\sigma/\partial k_j$, $j = 1, 2$, is the group velocity defined previously. Thus on a path defined by

$$dx_j/dt = C_{gj} = \partial\sigma/\partial k_j \tag{6}$$

the wavenumber vector suffers refraction because of nonhomogeneity in the environment. However, on this path, since $d\sigma/dt = (\partial\sigma/\partial k_i)(dk_i/dt) + (\partial\sigma/\partial x_i)(dx_i/dt) = 0$ by (5b) and (6), the frequency is constant. Given initial values, position and wavenumber vector, (5b) and (6) are readily integrated forward or backward in time. The resulting trajectory indicates TRW energy path. The constancy of σ not only constrains the ray paths (as we will see), but also serves as a useful check on the numerics.

3. A primitive equation model of deep-flow forcing by Loop Current and Loop Current eddies

The Princeton Ocean Model is used in an orthogonal curvilinear grid system that covers the region west of 55°W in the Atlantic, including the Caribbean Sea and the Gulf of Mexico (Fig. 2a). Steady inflow and outflow transports are specified at 55°W (W. J. Schmitz 2001, private communication; see also Schmitz 1996). These transports determine the depth-integrated (two-dimensional) velocities at the boundary, and are meant to account for the large-scale transports (wind-curl Sverdrup + thermohaline) through 55°W. The three-dimensional velocity, temperature, and salinity fields are then obtained through the open-boundary specifications described in Oey and Chen (1992). The annual-mean temperature and salinity values from Levitus and Gelfeld (1992) are specified at grid points where flows are westward (i.e., inflow), and advected using one-sided difference scheme where flows are eastward. The three-dimensional velocities are then determined using radiation conditions. These open-boundary specifications also set the baroclinic structure, which in the present case is largely geostrophic through the thermal-wind balance. They are sufficient to determine the interior

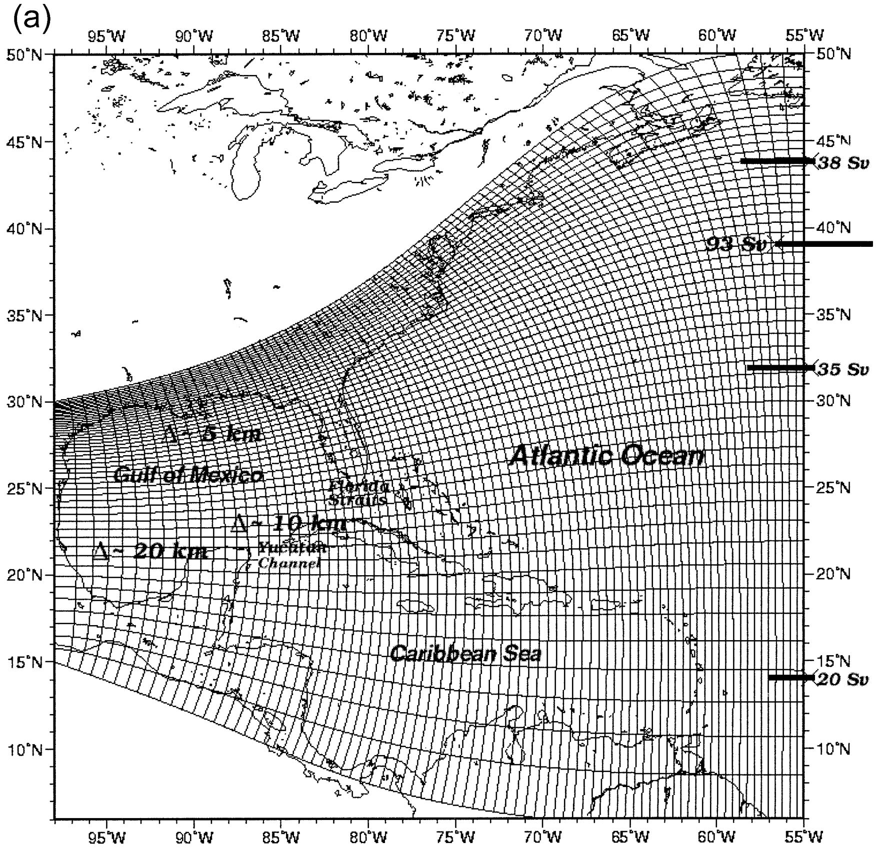

FIG. 2. (a) The model orthogonal curvilinear grid domain encompassing the entire Gulf of Mexico and Caribbean Sea and a portion of the Atlantic Ocean. Grid lines are shown at every seventh grid point. The approximate distribution of grid sizes in the gulf is indicated, and there are 25 sigma levels in the vertical, with vertical grid sizes less than 5 m near the surface over the deepest region of the gulf (~3500 m). A time-independent inflow and outflow transport profile, as a function of latitude (y), is specified across the 55°W as shown schematically. Details are in L.-Y. Oey et al. (2002, unpublished manuscript). For the process-study experiment described in this paper, all surface fluxes are zero. (b) The portion of the model domain and topography in the Gulf of Mexico. Isobaths are in meters, and shaded regions are where the topographic gradient $|\nabla h|$ is greater than 1.5×10^{-2}, i.e., 1500-m depth change in 100 km. (c) Contours of the topographic gradient $|\nabla h| \times 10^3$.

field: Caribbean inflow, Loop Current and eddies, and the Gulf Stream and its recirculation gyre. This open boundary specification is sufficiently removed from the gulf that free dynamical interaction between the Caribbean Sea and the gulf through the Yucatan Strait is retained (O96).

Details of the topography and the absolute values of its gradient in the gulf are shown in Figs. 2b,c. Steep topographic slopes, with maximum $|\nabla h|$ values as high as 0.05 are seen off west Florida and Yucatan northern shelves. Over these regions, the model may allow shorter-period (<10 days) TRW fluctuations. However, we believe that a good study of these steep regions would require a model resolution that is at least doubled that used here. Our present interest, therefore, is with the gentler topographic slopes over the north-central gulf, approximately along the 3000-m isobath (Fig. 2).

POM uses the so-called sigma transformation in the vertical, and we use 25 sigma levels with finer resolution over the upper and lower 500–1000 m of the water column, so that LC and LCEs, the forcing, and bottom-trapped TRWs, the response, can be better modeled. The horizontal grid sizes vary from about 10 km in the vicinity of the LC to 5 km in the northern gulf and 20 km in the southwestern corner of the gulf. The grid resolution over the LC and northern and central gulf is at least double that used by O96 (who used a uniform 20 km). To remove ambiguity when interpreting the origin of the forcing to deep flows, all surface fluxes are zero. In the model (as in O96), the energy source for deep EKE comes primarily from LC and LCE variability.

The σ-level pressure gradient error (Haney 1991) in the model is reduced by removing the basin-averaged density distribution (i.e., in z only) from the time-dependent density field before evaluating the pressure gra-

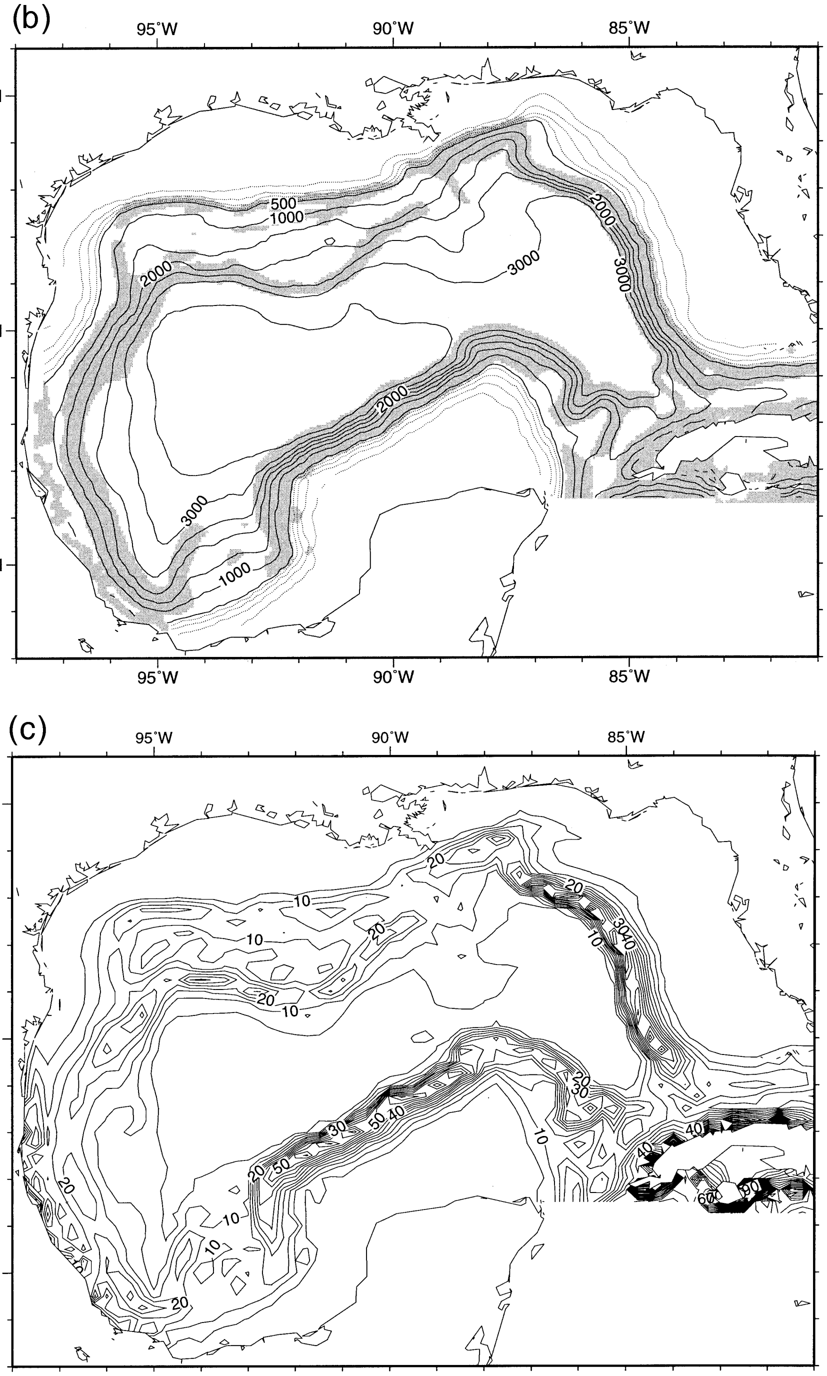

FIG. 2. (*Continued*)

dient terms (Mellor et al. 1994, 1998). Rigorous error evaluation during the course of integration is difficult. Nevertheless, a 1-yr test calculation using initially level density field $\rho_a(z)$ (horizontally basin-averaged annual-mean density) with small perturbation—that is, $\rho = \rho_a(z) - 0.1 \exp(z/1000 \text{ m}) \text{ kg m}^{-3}$ (Mellor et al. 1998) and zero (surface and boundary) forcing—was conducted. This yields a maximum current (the error) that goes asymptotically to less than 1.5 mm s^{-1} after 60 days, which as we will see is negligible in light of the speeds that range from a few centimeters to 1–2 meters per second typically found in the model gulf.

The model is initialized with an ocean at rest and is run in diagnostic mode for one month, during which the density field (ρ) is fixed at its annual-mean distribution. A (predominantly) geostrophically adjusted velocity

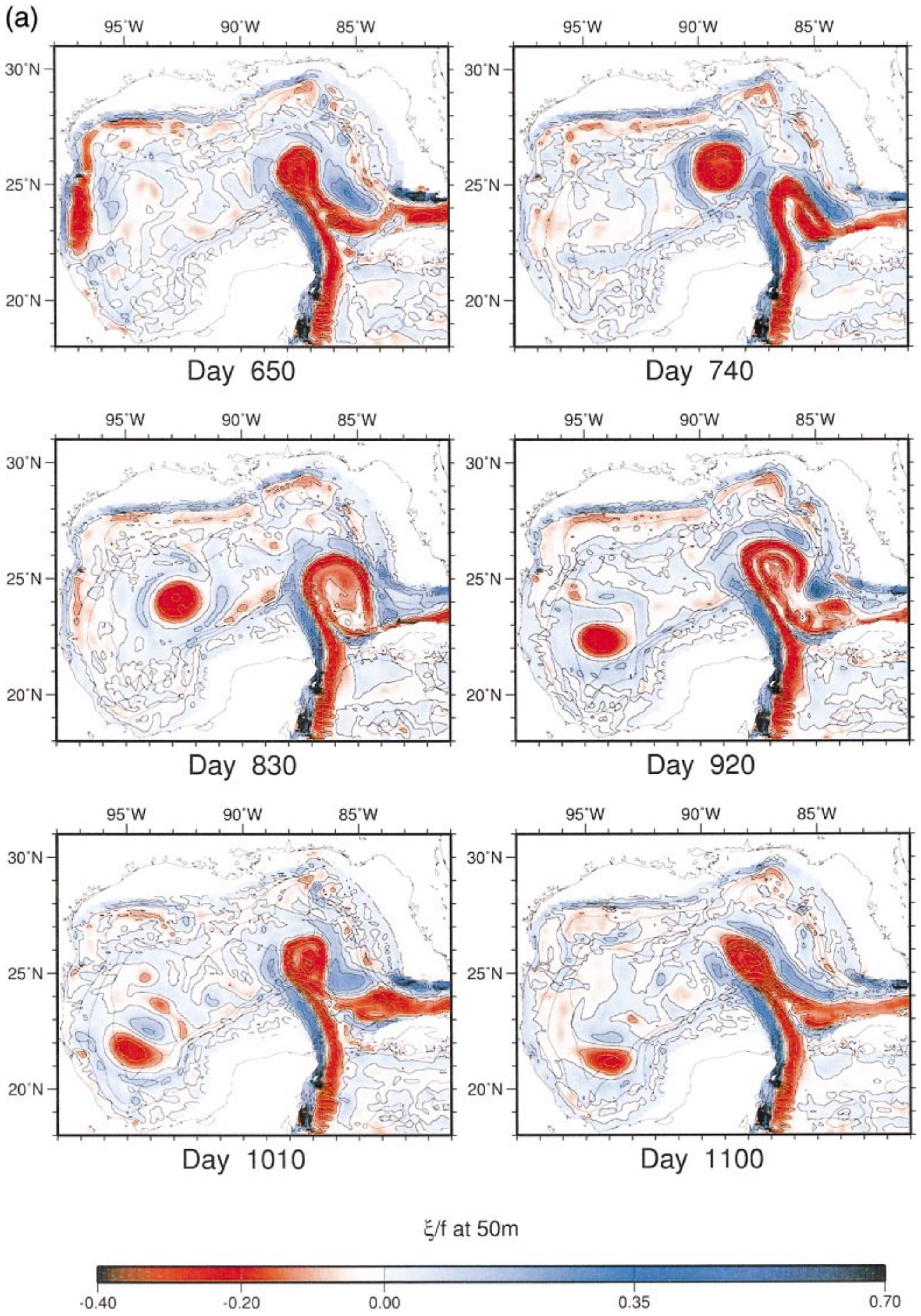

FIG. 3. (a) Ninety-day snapshots of relative vorticity (ζ/f; 5-day averaged) at $z = -50$ m, showing LCE shedding, southwestward propagation, and decay. (b) Time–latitude contours of free-surface elevation η along 90°W, showing passages of Loop Current eddies when η maximizes to about 0.3 m. Regions where $\eta > 0$ are shaded.

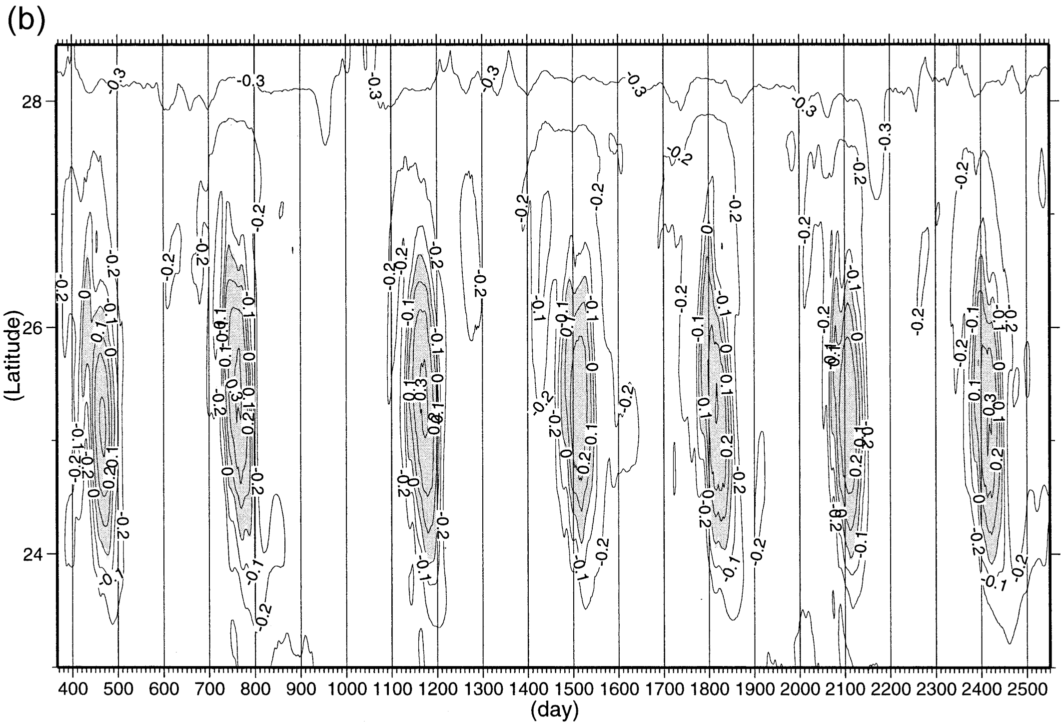

FIG. 3. (*Continued*)

field is established during this time. The prognostic calculation is then initiated from this balanced field and a quasi-equilibrium state, in which regular, nearly periodic LCE shedding occured, is established in about 2 yr. The integration is then continued through the 10th year. Smagorinsky's (1963) horizontal mixing formulation is used with its constant = 0.1, and ratio of horizontal diffusivity to viscosity is 0.1. Figure 3a gives snapshot examples (every 90 days) of contours of ζ/f (relative vorticity divided by local Coriolis parameter) at $z = -50$ m, showing LCE shedding and westward propagation. Figure 3b plots time–latitude contours of free-surface elevation η along 90°W, showing passages of LCEs when η maximizes to $\sim$0.3 m. Various characteristics of the LC and LCEs are as follows. The shedding period is nearly constant at 9–10 months (Fig. 3b) and LCE diameters are about 300 km. Once shed, modeled eddies traverse across the gulf in a southwestward direction at speeds of approximately 4–5 km day^{-1} and decay eventually in the southwestern corner of the gulf. In this constant-inflow experiment, the basic shedding mechanics and eddy kinematics follow closely those described in Hurlburt and Thompson (1980; cf. Sturges et al. 1993; O96). Typical swirl speeds and ζ/f around an eddy are 1.2 m s^{-1} and -0.4, respectively, while the corresponding values at the western edge of the LC in the Yucatan Strait are 1.5 m s^{-1} and 0.7. The maximum swirl speeds are weaker than those typically observed, about 1.5–2 m s^{-1} (Kirwan et al. 1988; Forristal et al. 1992). The resulting weaker forcing will likely result also in weaker deep response. This should not however, seriously jeopardize our attempt to diagnose and study TRWs, which basically are linear waves. On the other hand, the maximum modeled swirl speeds represent improvements over those found in O96, which gives values of 0.76 m s^{-1} ($\zeta/f \approx -0.25$). Since the forcings are similar in the two calculations, the improvements are a result of increased grid resolution (doubled) in the present case (cf. Oey 1998).

While the near-periodic shedding and constancy of direction of LCE propagation are idealized settings not found in the real ocean, they represent dynamically consistent forcing for (deep) flow EKE in the gulf. By understanding how TRWs develop in this simplified system, we hope to develop hypotheses and ideas for future analyses of more realistic models, and of observations as well.

Model data processing

For the purpose of identifying TRWs in the PE model, we find it useful to divide the model's results into four isopycnal layers, with layer 1 from surface to $27\sigma_t$ ($\sim$300 m thick), layer 2 from $27\sigma_t$ to $27.5\sigma_t$ ($\sim$500 m thick), layer 3 from $27.5\sigma_t$ to $27.7\sigma_t$ ($\sim$500 m thick), and layer 4 from $27.7\sigma_t$ to bottom (thickness $\approx$ 1000 m or more). Figure 4 shows an example of this division at 90°W. Since TRW motions are columnar (vertically coherent) at depths below about 1000 to 1500 m, we examine EKE in the fourth layer, that is, below the

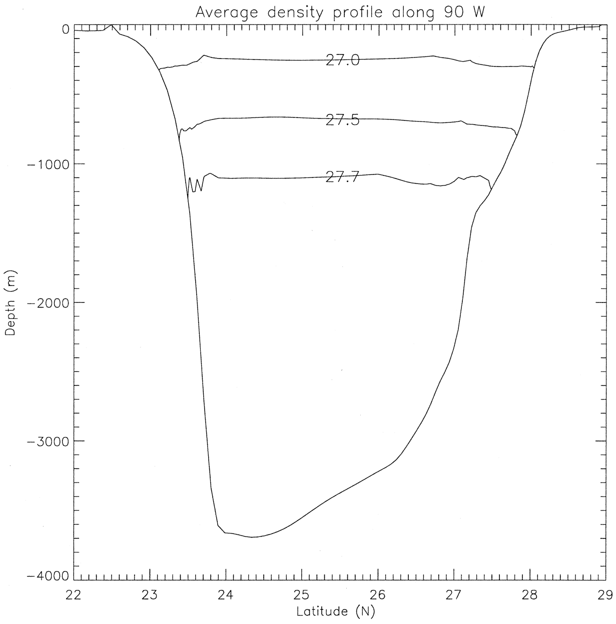

FIG. 4. A time-averaged cross-sectional contour plot of density at 90°W that describes isopycnal division of the model's three-dimensional field into four layers: layer 1 from surface to $27\sigma_t$, layer 2 from $27\sigma_t$ to $27.5\sigma_t$, layer 3 from $27.5\sigma_t$ to $27.7\sigma_t$, and layer 4 from $27.7\sigma_t$ to bottom.

$27.7\sigma_t$ surface (note that this lies approximately 1000 to 1500 m below the free surface). The modeled currents are daily averaged, then depth averaged in each layer. The depth averaging in the fourth layer precludes possible biases (of high EKE) that might occur in some region if a fixed z level were used to search for TRWs. It has the added nicety of also eliminating any gridpoint noise. (On the other hand, the depth averaging *reduces* by at least 50% the values of the near-bottom kinetic energy.) The last 7 yr of the 10-yr run were then spectrally analyzed, and the results in the 20- to 100-day TRW band were examined.

4. Deep-flow eddy kinetic energy

In this section, we determine in the PE model regions where TRWs are active in the gulf. To do this we first search for areas where a significant (60%) part of the total energy falls in the TRW period range of 20–100 days, where the deep energy is above a certain threshold, and where bottom intensification exists. We then check that these regions are where the topographic slopes and stratification are such that the 20–100 days TRWs can be supported. We next calculate spatial correlation to examine, in an ad hoc way, wave propagation in these regions of significant deep energy. We then utilize the TRW dispersion equation [(1)] and integrate the ray equations [(5b) and (6)] [or (B3) and (B6) when deep mean currents are included], to show that rays originate in the LC and LCEs, and are confined in these significant deep energy regions.

Figure 5 compares the time series of lower-layer (i.e., layer 4) kinetic energy fluctuations (LOKE) at a station just west of the LC (25.8°N, 88°W) with the corresponding 20–100-day band-passed LOKE (henceforth referred to as $\mathrm{LOKE}|_{20\text{–}100\mathrm{d}}$). At this station the amplitude and phase of the band-passed series generally follow those of the total series. The ratio of their standard deviations, $\mathrm{LOKE}|_{20\text{–}100\mathrm{d}}/\mathrm{LOKE}$ (note that here the same notation "LOKE" is used for standard deviation) ≈ 0.68. P. Hamilton (2001, personal communication) found that, where TRWs are observed over the continental slope of the gulf, they generally account for some 95% of the total near-bottom EKE. In the present case in which the energy is averaged over the lower layer (thickness ~1000–2000 m assumed > TRW trapping scales; see below), the appropriate percent value assuming TRW exponential decay with height above the bot-

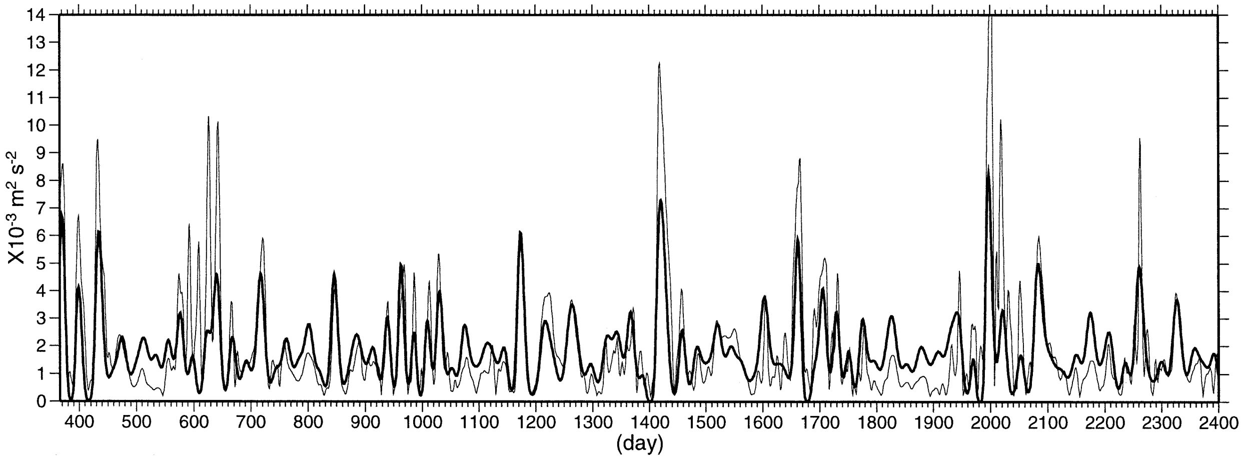

FIG. 5. A comparison of the time series of lower-layer (layer 4) kinetic energy (LOKE; thin curve) at a station just west of the LC (25.8°N, 88°W) with the corresponding 20–100-day band-passed LOKE ($\mathrm{LOKE}|_{20\text{–}100\mathrm{d}}$; thick curve).

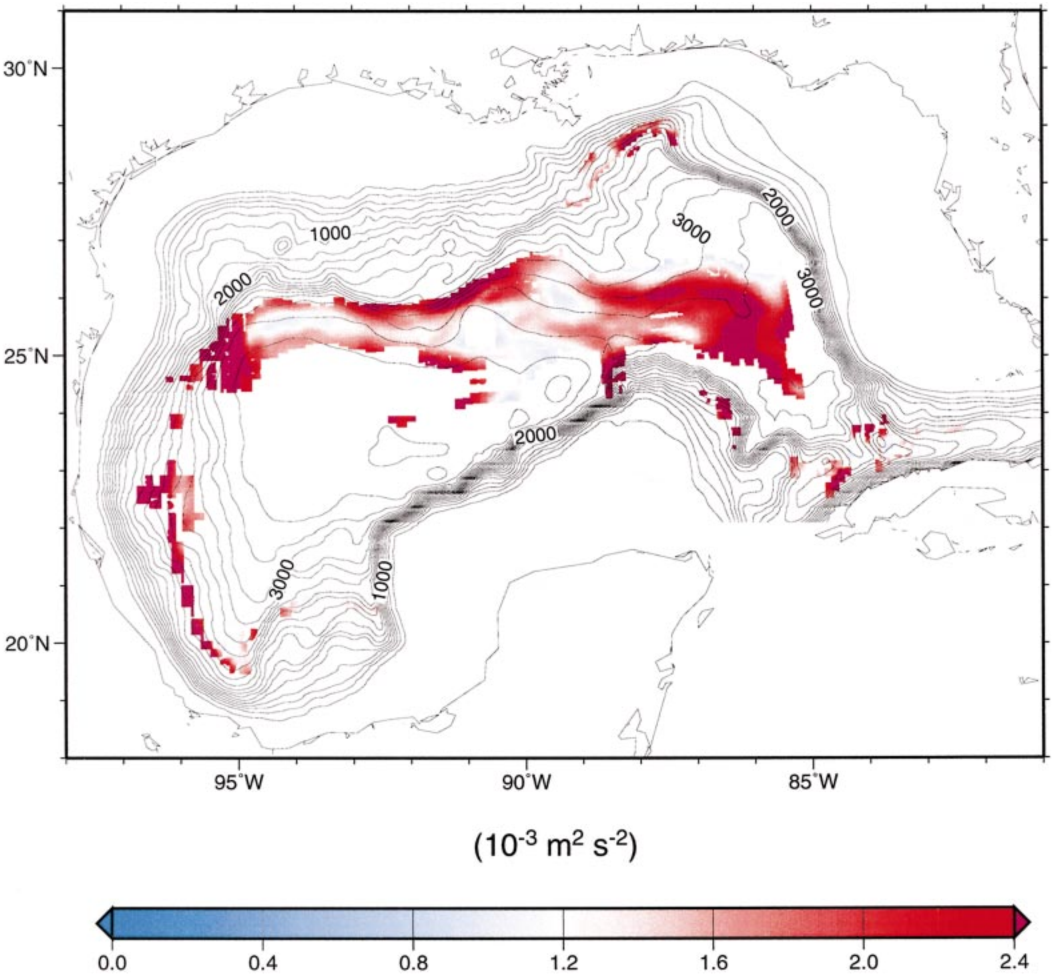

FIG. 6. The lower-layer kinetic energy in the 20–100-day periods (LOKE$|_{20\text{–}100\text{d}}$). Regions where the ratio of LOKE$|_{20\text{–}100\text{d}}$ to total LOKE is less than 60%, where there is no bottom intensification, and where LOKE does not exceed the gulfwide average of 10^{-3} m^2 s^{-2} are omitted as discussed in the text.

tom (from a maximum of 95% at bottom) is $\approx (1 - e^{-1}) \times 0.95 \approx 60\%$. Thus Fig. 5 suggests that, at least at this location, TRWs *may* exist. We therefore consider only those regions where LOKE$|_{20\text{–}100\text{d}}$/LOKE $> 60\%$. To avoid regions where the ratio is artificially inflated, we impose a second, minimum-LOKE constraint that the local LOKE exceeds 10^{-3} m^2 s^{-2}, the gulfwide-averaged standard deviation of LOKE. A third constraint is also imposed such that we only consider those regions where the kinetic energy shows intensification near the bottom (Hamilton 1990). These constraints are probably overrestrictive in that they will likely eliminate potential sites (for TRW activities) where both TRW and strong locally forced, non-TRW components of the EKE coexist, under the LC for example. Thus, while the minimum-LOKE constraint is satisfied, the ratio and bottom-intensification requirements may not be. On the other hand, the constraints ensure that what survive are robust features of the model that may have better chance of being observed in the real ocean.

Figure 6 gives LOKE$|_{20\text{–}100\text{d}}$ after the above three constraints are imposed. The figure shows significant LOKE$|_{20\text{–}100\text{d}}$ region across the gulf over approximately the 3000-m-isobath. We will focus on this along-3000-m-isobath band of LOKE$|_{20\text{–}100\text{d}}$ and will refer to it as the ‘‘CGKE,’’ or central-gulf LOKE$|_{20\text{–}100\text{d}}$ band. While there are other significant LOKE$|_{20\text{–}100\text{d}}$ regions in the model gulf (e.g., 28°N, 88°W, Fig. 6), the central-gulf band suggests a *simpler* cause-and-effect scenario—that is, forcing under the LC and southwestward propagating LCEs, and near-bottom energy that spreads westward. We comment that the CGKE band not only indicates regions where LOKE$|_{20\text{–}100\text{d}}$/LOKE $> 60\%$, it also coincides well with areas where bottom intensification exists in the model gulf. In other words, the extent and shape of the band in Fig. 6 are essentially unchanged if we were to impose only the bottom-intensification (and minimum LOKE) constraint.

We now check that the CGKE band resides in a region where TRWs can be supported. We use (2) to plot con-

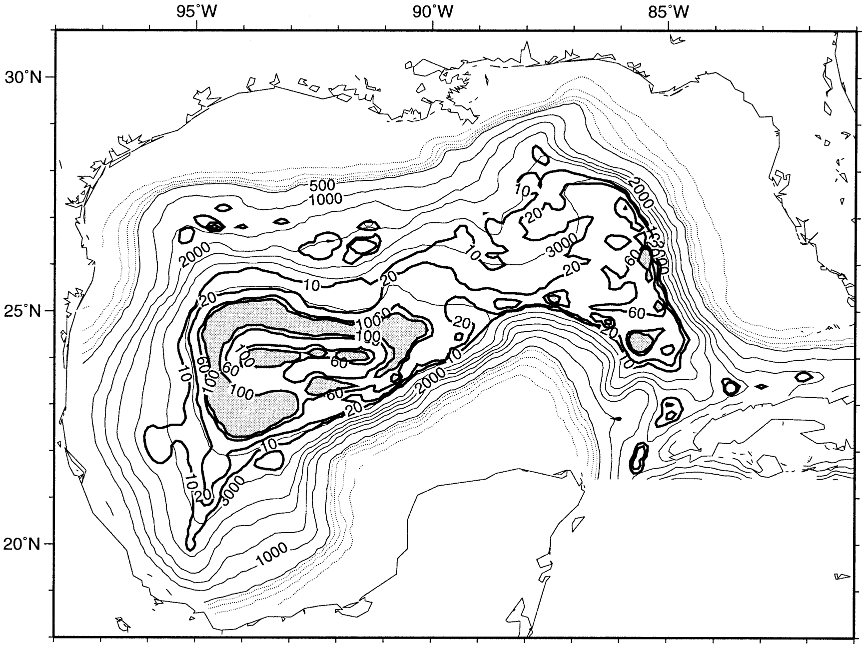

FIG. 7. Contours of the minimum period (days) $P = 2\pi/\sigma \le \tanh(NhK/f)/(N|\nabla h|)$ allowed by the TRW dispersion relation, for N given in Fig. 10 and $2\pi/K = 110$ km. Regions that cannot support TRWs with periods shorter than 100 days are shaded.

tours of the minimum period $P = 2\pi/\sigma \le \tanh(NhK/f)/(N|\nabla h|)$. Figure 7 shows P for $2\pi/K = 110$ km, and using $N(x, y)$ derived from the model as explained below. Except for the relatively gentle topography of the deep central gulf where only long-period (>100 days) TRWs can be supported, waves of shorter periods can in theory exist almost anywhere in the gulf. It is therefore not immediately apparent why $\mathrm{LOKE}|_{20\text{–}100\mathrm{d}}$ is confined only along the narrow band over approximately the 3000-m isobath in Fig. 6. In other words, why is there not a more expansive (north–south) spread of energy that exhibits TRW characteristics to other regions of the gulf? The answer lies in the way that TRW energy is refracted. In the following, we use two methods to attempt linking the CGKE band with TRWs: first a somewhat ad hoc phase and correlation analysis, and second a more precise ray (energy) tracing calculation. We then discuss the sources of these near-bottom EKE.

a. Phase and correlation analysis

We computed time-lagged correlations of the $\mathrm{LOKE}|_{20\text{–}100\mathrm{d}}$ time series at 25.8°N, 88°W (i.e., Fig. 5) with all other grid points, chosen as we see later because it is near the generation site of TRWs. The top panel of Fig. 8 shows contours of the lagged correlation (which differ from zero at the 95% confidence level) in the CGKE region, from 86°W to 92°W, and the lower panel shows the lags in days. The figure shows that the CGKE band coincides with region of significant correlation, with fair values = 0.45 at approximately 25.8°N, 92.2°W, a distance some 400 km west of the X point (the 95% significance level is ≈0.15 at this western point). In the vicinity of the X point, the time-lag contours suggest a *phase* propagation from northeast to southwest.[1] Since isobaths are approximately east–west in this region, the southwestward phase propagation is consistent with a southwest-directed or downslope wavenumber vector, hence northwest-directed or upslope group velocity that one would deduce from the TRW dispersion relation (section 2, also Fig. 1).

b. Ray-tracing calculations

The approximate coincidence of the region of significant correlation with the CGKE band suggests a ‘‘channeling’’ effect of near-bottom energy over the 3000-m isobath, perhaps related to refraction of TRWs. To study this we trace wave rays based on the QG dispersion relation (section 2). In addition to yielding information on various wave properties along the paths, the calculation will also help locate source(s) of TRWs. In the Gulf Stream region, the ray-tracing method has been used by Pickart (1995) to identify TRWs and TRW sources.

1) THE ENVIRONMENTAL FIELDS

The method requires specifications of four environmental fields: $N(x, y, z, t)$, $h(x, y)$, and the two components of $\nabla h(x, y)$. Implicit in section 2 is that these

---

[1] Strictly speaking, time-lag contours and phase lines are equivalent only for monochromatic waves.

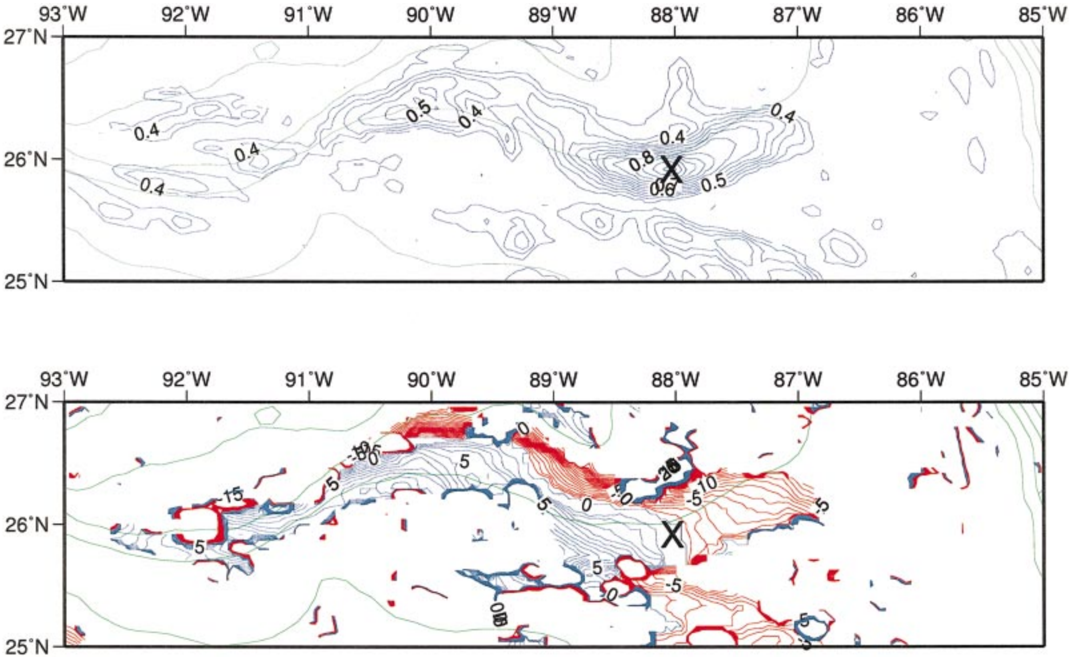

FIG. 8. (top) Contours of maximum lagged correlation (at 95% significance level) in the vicinity of the 3000-m isobath (contour interval is 500 m), CGKE band (see text), from 86° to 92°W. (bottom) The corresponding lags in days (positive in blue; negative in red).

variables are slowly varying with space and time (Lighthill 1978; see also Hogg 1981 in oceanographic context). The topography was smoothed using a Gaussian-type interpolator (Oey et al. 2001) with a ''radius of influence'' of 0.6°, comparable to the filter width of 150 km used by Pickart (1995). Figure 9 compares the smoothed topography with the original one used in the numerical simulation. The smoothing removes short-scale topographic irregularities but leaves the large-scale features (and also those of ∇h, not shown) essentially intact. To obtain a smoothed N, we performed time and depth averaging over the last 7 yr of the 10-yr simulation, and also for depths below the $27.5\sigma_t$ surface (i.e., in layers 3 and 4). The resulting contours of $N(x, y)$ are shown in Fig. 10. Note that over the CGKE band, $N \approx 10^{-3}\ \mathrm{s}^{-1}$ (uncertainty in this value will be discussed below). These smoothed values (N and h) are interpolated onto a longitude–latitude grid with constant grid sizes ($0.01° \times 0.01°$), on which we calculate ∇h using finite differences. Note that the uniform grid is used for calculating the environmental fields only and does not define the actual coordinates of rays.[2] The ray equations [(5b) and (6)] are integrated using the fourth-order Runge–Kutta method with adaptive step size (Press et al. 1992).

In addition to $N(x, y, z, t)$, $h(x, y)$, and $\nabla h(x, y)$, deep currents $\mathbf{u}_{\mathrm{deep}}$ also affect ray paths. The modifications to (5b) and (6) are given in appendix B. As for N, a 7-yr averaging was performed on the modeled currents at 200 m above the bottom. The resulting $\mathbf{u}_{\mathrm{deep}}$ is used in the ray calculations based on equations (B3) and (B6) to assess the effects of deep mean flows on TRW propagation.

2) DETERMINING THE RAYS' INITIAL POSITIONS AND WAVENUMBER VECTORS

To integrate (5b) and (6) [or (B6) and (B3), same below], initial position (x_0, y_0) and wavenumber vector (k_0, l_0), as well as the frequency σ defined for each ray, must be assigned. By integrating the equations backward (inverse ray tracing; Pickart 1995) from positions in the CGKE band, test calculations with various (k_0, l_0) [at period = 64 days, $-0.125 < l_0 < -0.03\ \mathrm{km}^{-1}$ and $|k_0| \ll |l_0|$, where here the direction of l_0 is opposite to that of the local ∇h; thus hodograph ellipses are predominantly aligned with the local isobaths; Hamilton (1990)] satisfying the dispersion equation indicate that rays consistently trace back to locations under the LC and around the northern edges of the southwestward propagating LCEs. These tests suggest that LC and LCE variability are the prime drivers of the lower-layer fluctuations found in the PE model. With these tests serving as a rough guidance, six initial positions, (x_0, y_0), shown as ''+'' in Fig. 11a, are chosen, and the ray equations are then integrated *forward* with a set of (k_0, l_0) determined from the PE model outputs as follows. For convenience, the stations and corresponding rays will

---

[2] The use of an east–west and north–south grid, rather than the original orthorgonal curvilinear grid of POM, simplifies the application of TRW relations given in section 2.

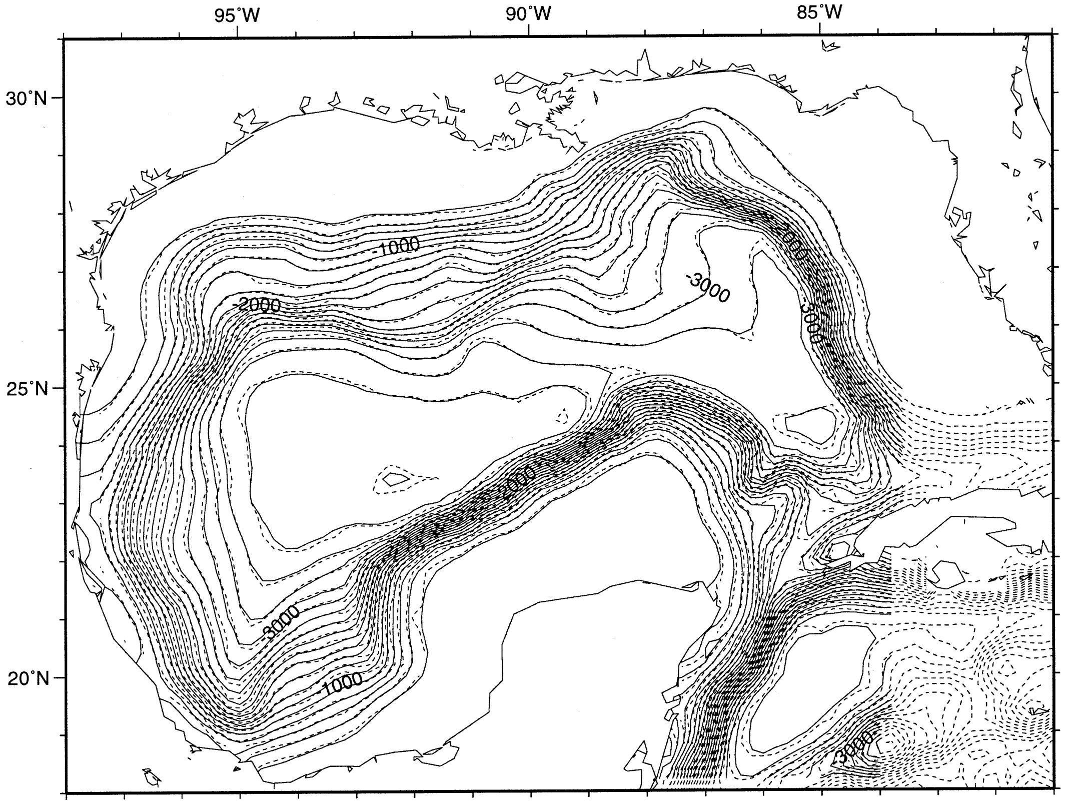

FIG. 9. A comparison of the smoothed topography (m) used in the ray-tracing calculation with the original one used in the numerical simulation.

be referred to consecutively from east to west as station/ray 1 through station/ray 6.

In the vicinity of each initial position, energy spectra at a cluster of n stations [we used $n = 10$, including (x_0, y_0)], and hence their phases at each frequency, are computed. Any three stations then give at least two linearly independent equations for two unknowns k and l. The set of k and l thus solved from all (nonredundant) triad permutations are then averaged. Figure 12 shows an example, at station 2 (see Fig. 11a), of four such solutions plotted on the dispersion curves for four frequencies. The frequencies were chosen to correspond to spectral peaks at this and its surrounding nine stations, at periods ≈ 32, 42.7, 51.2, and 64 days (cf. O96). The results at other stations are similar. The wavelength values range from 63 to 210 km and they are averaged for each period. Figure 12 shows that the averaged solution (k_0, l_0) pairs correspond to wavelengths $2\pi/K \approx 85$ to 150 km for the four selected periods. Moreover, they reside within the linear portion of the dispersion curves; that is, they approximately satisfy (2) with $\beta \approx 0$ and when $\tanh(NhK/f) \approx$ constant. Thus for each frequency, only the ratio k_0/l_0 (i.e., the angle θ) is relevant. Thus while group speeds increase with increasing wavelengths [(3)], ray paths are relatively insensitive to wavelength (see below). In the following, we use $2\pi/K = 110$ km for the "benchmark" calculation; (2) then yields a first-guess value of either k_0 or l_0, and is used in an iterative process to solve (1) for more precise values of k_0 and l_0. Hamilton (1990) estimates from observations (his Table 2) wavelengths from 110 to 300 km for TRW periods from 18 to 300 days. Thus the wavelength values estimated from the PE model are on the lower end of observed, and we will later evaluate the sensitivity of the ray solution to larger wavelengths.

3) RESULTS AND INTERPRETATIONS

In Fig. 11a, an example of six rays emanating from initial stations marked "+" is shown superimposed on 10-yr assemblage contours of $\zeta/f = -0.2$ at $z = -50$ m. This value of ζ/f is used as it indicates well the outer rim of the LC and LCEs. The contours show the predominantly southwestward propagation of LCEs from their initial birth place in the LC. Each ray is integrated for 100 days with a period of 64 days, and on each one we plot at the 10-day interval the wavenumber vector direction with length proportional to its *wavelength.* Rays at periods 32, 42.7, and 51.2 days (Fig. 12) have also been tested, and the results will be commented upon later.

Rays 1 and 2 originate from under the region of active LC north–south pulsation and LCE shedding. At station 1, topographic slope is weak, and $\beta_{\text{Topo}}/\beta = f|\nabla h|/$

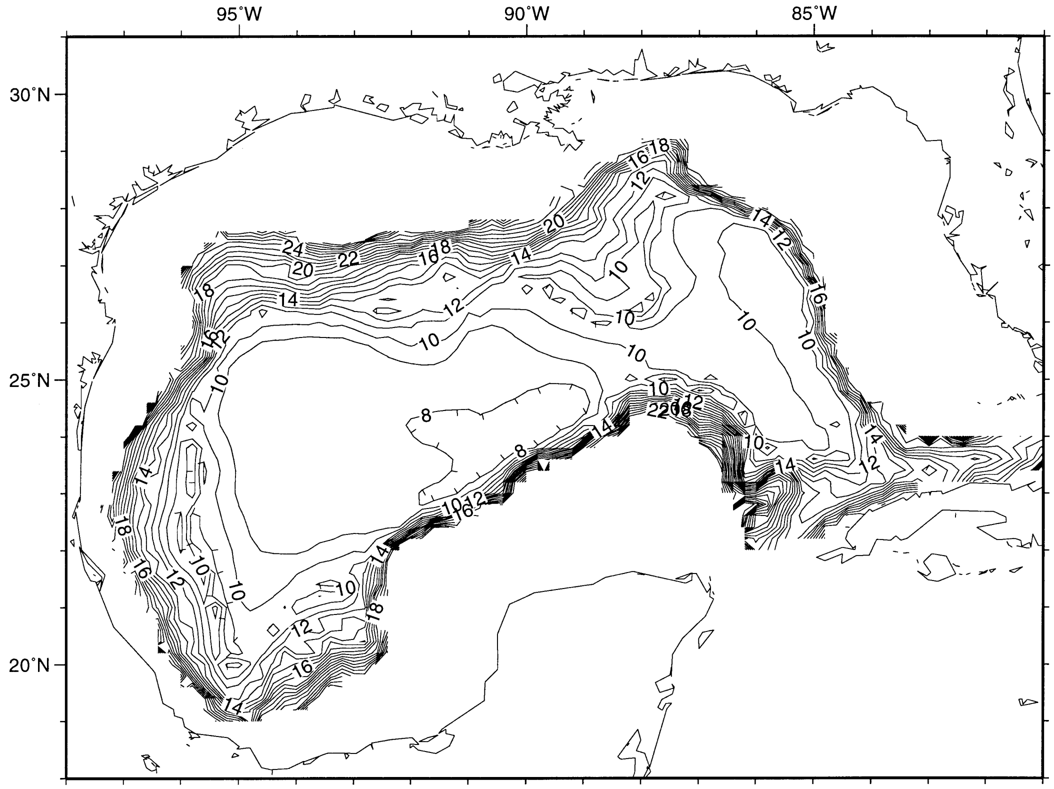

FIG. 10. The time (over the last 7 yr of the 10-yr simulation)- and depth (for depths below the $27.5\sigma_t$ surface)-averaged Brunt–Väisälä frequency N (10^{-4} s^{-1}). This smoothed N, unless otherwise indicated in text, is used in the ray-tracing calculation.

($h\beta$) $<$ 1. Waves that emanate from here are at first predominantly planetary and propagate slowly (~ -3km day^{-1}). It later converges with ray 2, which we detail below.

At station 2, $\beta_{\text{Topo}}/\beta \approx 6$, and ray 2 follows closely the 3000-m isobath, crosses over it, but remains just inshore of it as the ray continues to the western gulf. Its path, together with that of ray 1, coincides closely with areas of significant LOKE$|_{20\text{–}100\text{d}}$, from about 87°W through approximately 92°W (Fig. 11a, lower panel). West of 92°W, the wavelength shortens to values $<$30 km, which is too short to be resolved by the PE model (this portion of the ray is of lighter shade in Fig. 11a, top panel). The lower panel of Fig. 11a (or Fig. 6) also shows areas along the 3000-m isobath where LOKE$|_{20\text{–}100\text{d}}$ attains local maxima: near station 2 or the "source," and near 91°W, 94°W, and 95°W where rays converge. The ray equations can be used to explain the channeling effect (of LOKE$|_{20\text{–}100\text{d}}$) over the 3000-m isobath, mentioned previously, and also why TRW wavelengths shorten westward. Specifically, we can explain why the ray must bend from propagating northwestward to southwestward at about the 90°W, and why farther west it stays inshore of the 3000-m isobath and does not veer northward crossing the 2000-m isobath. Since $\beta_{\text{Topo}}/\beta$ remains $\gg 1$ (see Fig. 11b and discussion of it below), (2) is an excellent approximation to the dispersion relation. Thus,

$$\sigma = N|\nabla h| \sin(\theta)/\tanh(NhK/|f|) \approx N|\nabla h| \sin(\theta), \quad (7)$$

where recall that θ is the clockwise angle the wavenumber vector makes with the direction of steepest topographic descent (i.e., with $\nabla h/|\nabla h|$; Fig. 1). [Also, for $NhK/|f| \approx O(1)$ or larger, the tanh is a weak function of $NhK/|f|$ and the first form of (7) is good with tanh $\approx$ constant.] Since σ is constant along a ray, $\sin(\theta)$, and hence θ (which remains in the first quadrant; i.e., $\theta < 90°$), must decrease as the ray enters regions of steeper topographic slopes and/or stronger stratification. In other words, the wavenumber vector must become more *perpendicular* to, and the ray path [which points in the direction of the group velocity; see discussion preceding (3)] more *aligned* with, the local isobaths. Figure 2b shows that the topographic slope becomes steep between the 2000- and 3000-m isobaths west of 90°W. This, coupled also with increasing (though slight) stratification to the north (Fig. 10), explains why the ray must turn from northwestward to southwestward around 90°W, and must confine itself between the 2000- and 3000-m isobaths farther west. The agreement of this channeling or focusing effect of the ray path and the CGKE band lends supports that the latter is a manifestation of TRWs contained in the PE model.

We can also explain how wavelengths are shortened by refraction as TRWs propagate northwestward into

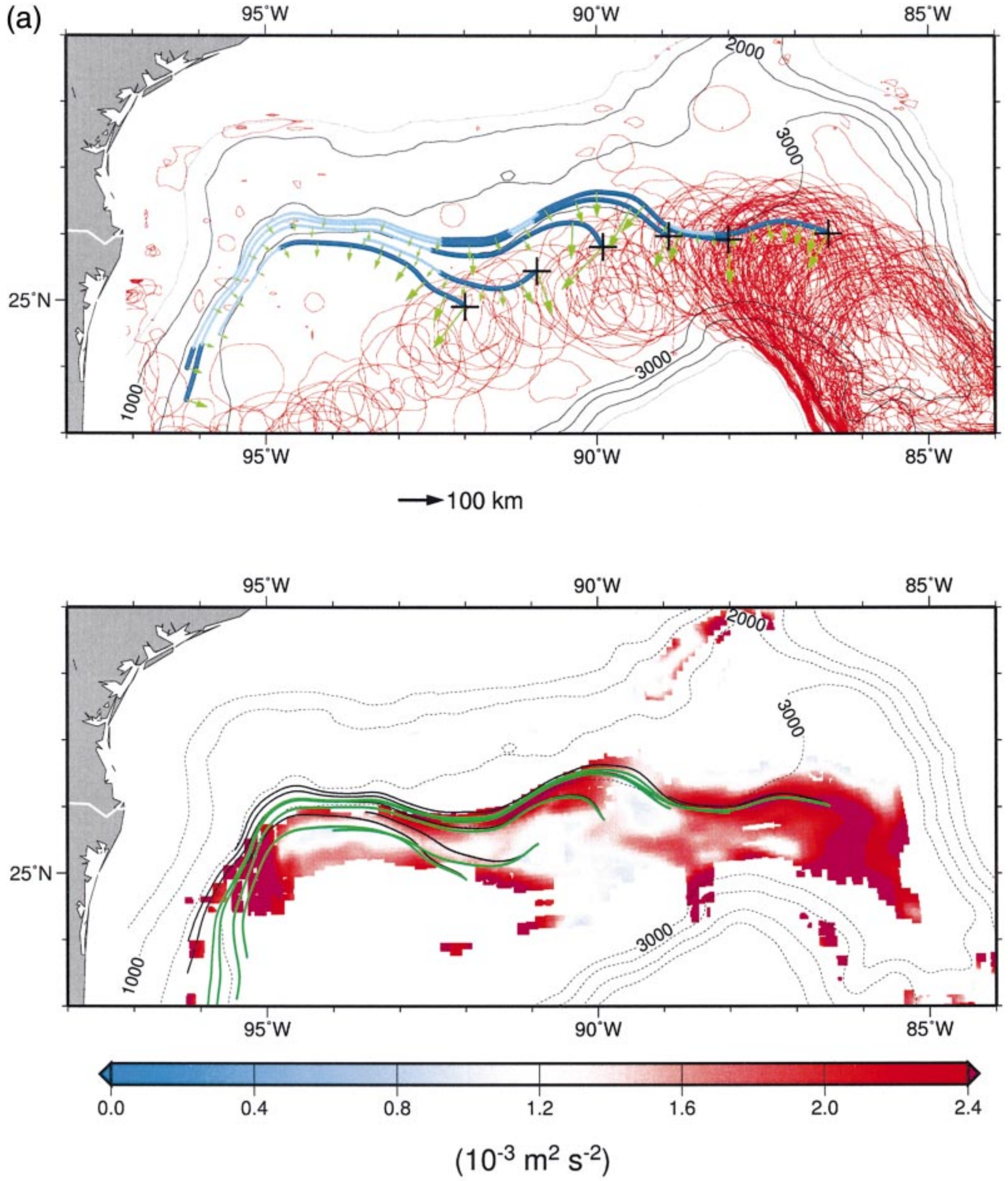

FIG. 11. (a) (top) Wave rays (in blue; lighter blue for wavelength $<$ 30 km) traced using the TRW dispersion relation indicating deep energy paths in the gulf that originate under the Loop Current and Loop Current eddies. The outer rims of LC and LCEs are indicated in red by the 10-yr assemblage of the $\zeta/f = -0.2$ contours at $z = -50$ m obtained from the PE model. The green arrows indicate wavenumber vectors, plotted every 10 days along the path, with lengths equal to *wavelengths* (the 100-km scale is shown below the panel). (bottom) The 20–100-day deep energy from Fig. 6 (scale at bottom). Superimposed is a comparison of rays from the top panel (thin solid) with those derived by including effects of deep mean flow [thick green curves, using (B6) and (B3)]. (b) Various TRW and ambient properties along ray 2 (defined in text) of (a): (left, from top to bottom) 1) East–west (solid) and north–south (dashed) group velocity components, and corresponding group velocity magnitude (dash–dot); 2) Brunt–Väisälä frequency; 3) topographic gradient (solid; left y axis) and ratio of topographic to planetary beta, $\beta_{\text{Topo}}/\beta = f|\nabla h|/(h\beta)$ (dash; right y axis); and 4) wavenumber vector (k, l) variation. (right, from top to bottom) 1) Wavelength; 2) water depth (solid; left y axis), trapping scale (dash; right y axis), and estimates from the PE model results at five locations along ray 2 (full circles; see Fig. 13); 3) lower-layer EKE in the 20–100-day periods; and 4) distance along the ray as a function of longitude. The dotted curves show respective properties corresponding to the ray that includes effects of deep mean currents (group speed in the top-left panel).

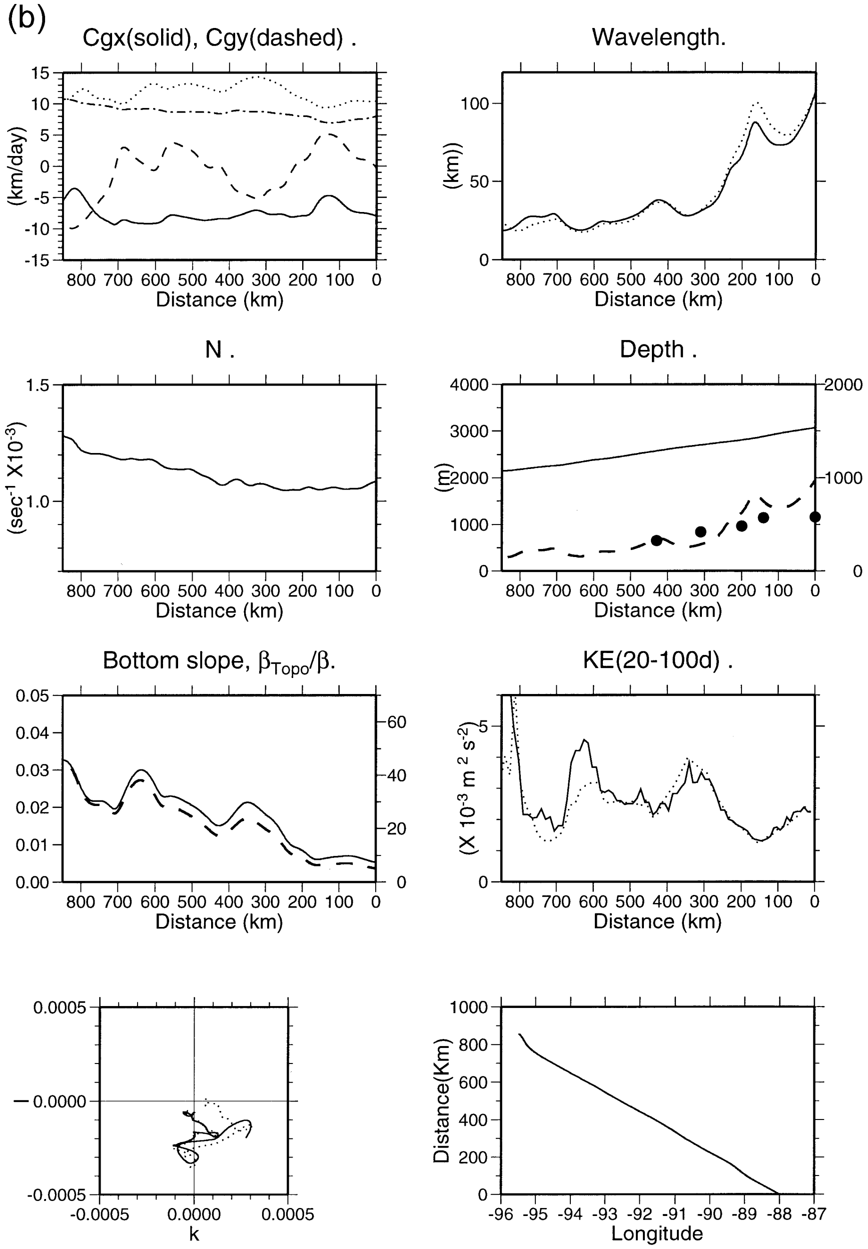

FIG. 11. (*Continued*)

regions of increasing topographic slope and stratification. One can multiply (5a) by k_i and use (7):

$$d(k_i^2/2)/dt = -l \sin(\theta)\partial(|h_y|N)/\partial y, \qquad (8)$$

in which we assume for simplicity that contours of h and N are predominantly zonal. It is clear from Figs. 2b and 10 that both $\partial|h_y|\partial y$ and $\partial N/\partial y$ are positive inshore of the 3000-m isobath so that since $l < 0$, $d(k_i^2/2)/dt > 0$ and TRW wavelength shortens along the ray.[3] Hamilton (1990) also noted westward shortening of TRWs from observations.

Figure 11b gives various properties along the ray path 2. The magnitude of the group velocity (dash–dotted curve in first left panel) varies from about 8 km day^{-1} at the initial location (station 2) to over 10 km day^{-1}

---

[3] Within the WKB framework, one can use a natural coordinate such that positive y points in the direction *opposite* to the vector ∇h, so that the argument is locally valid. Also, $N\partial|h_y|\partial y > |h_y|\partial N/\partial y$ for our case.

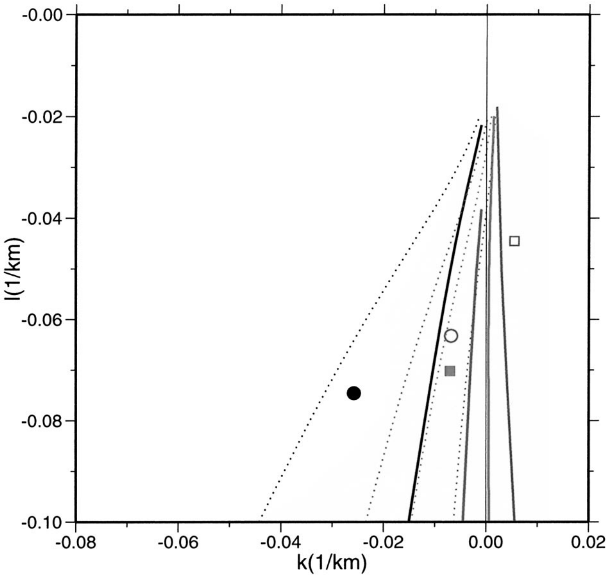

FIG. 12. TRW dispersion curves corresponding to peak spectral periods of (going from left dotted and solid curves to right curves) 32, 42.7, 51.2, and 64 days. Solid and dotted curves are for $N = 10^{-3}\ s^{-1}$ and $6.25 \times 10^{-4}\ s^{-1}$, respectively. The symbols denote averaged values derived from the PE model results at station 2 of Fig. 11a (filled circle, 32 days; open circle, 42.7 days; filled square, 51.2 days; and open square, 64 days).

as the ray turns southward along the Mexican–Texas slope, with an average of about 9 km day^{-1}. These values of the group speed are consistent with those reported by Hamilton (1990) and O96. The x component (C_{gx}) is negative through the entire ray path as wave energy propagates westward, while the y component (C_{gy}) attains both positive and negative values as the ray undulates in accordance with the location of steep topographic gradient as explained above. This undulation is also reflected by the changing sign of the x component of the wavenumber vector, k, shown on the bottom left panel, since this is very nearly perpendicular to C_{gy}. The TRW is continuously being refracted along the ray path and its wavelength shortens from an initial value of 110 to 30 km (first right panel). Besides Hamilton (1990) in the gulf, Pickart (1995) also found wave-shortening over the slope off Cape Hatteras. As noted above, topographic slope steepens (third left panel, solid) and topographic beta dominates on ray 2 as $\beta_{\text{Topo}}/\beta$ increases to over 40 near the western gulf (third left panel, dashed). The solid curve in the second right panel indicates decreasing water depth along the ray, while the dashed curve shows the vertical trapping scale μ^{-1} of the wave. Along the ray, this is very nearly proportional to the wavelength, as can be seen by comparing the first and second right panels and which follows directly from the linear theory for which the vertical structure $\sim\cosh(\mu z) \approx \cosh(NKz/f)$ from (1a). The values vary from about 1000 m at the beginning of the ray to 300 m some 300 km to the west. We may estimate the trapping scales from the PE model profiles of Fig. 13. Here we plot vertical profiles of the square root of the 20–100-day kinetic energy at five locations from east (A) to west (E) along ray 2. Excluding the very near-bottom boundary layer (<50 m) where the energy is low, the profiles all show energy decay with height from the bottom, to a minimum that probably represents the combined effect of the upper-ocean energy decay (i.e., first baroclinic mode) and the TRW decay from below. Apart from this complication, one may assume an exponential decay from each profile's maximum to its minimum, and estimate the corresponding e-folding decay height. The solid-circle symbols in the second right panel of Fig. 11b show the five estimated values. Though values differ,[4] the PE model results show also westward decreasing trend of the trapping scales (from 600 to 300 m) in agreement with the TRW solution. Last, the third right panel shows $\text{LOKE}|_{20\text{–}100\text{d}}$, the accumulated energy of not only those TRWs that originate at station 2 and propagate along ray 2 at the 64-day period, but also those of other rays. It illustrates energy increases due to ray focusing at the previously mentioned locations: 91°W, 94°W, and 95°W. One notes that these local maxima in $\text{LOKE}|_{20\text{–}100\text{d}}$ coincide with minima in wavelength (first right panel), a feature consistent with the linear wave theory that energy varies as squares of the wavenumber.

To get a sense of the bottom motions, Fig. 14 shows examples of vector stick plots at locations A (Fig. 14a) and D (Fig. 14b) of Fig. 13, upward from the near-bottom depth level where the $\text{LOKE}|_{20\text{–}100\text{d}}$ shows maximum (Fig. 13, bottom panel). The top panel shows vectors at a representative near-surface level, and y-directed sticks in these plots denote motions parallel to local isobath, positive clockwise around the gulf (i.e., generally eastward). Both locations show columnar (i.e., in phase) structures that decay with height in the lower 1000 m or so of the water column, and fluctuations in the 20–100-day periods can be seen. At location A, the motion appears uncorrelated with that near the surface. In other words, their relation, if any, cannot be seen in this plot of the whole motion (see, however, next section), since the near-surface motions are dominated by LC and LCE fluctuations. At location D, away from the direct influence of the LC and LCEs, the near-bottom and near-surface motions are more correlated, yet the former over a height of about 1000 m from the bottom is evidently more topographically controlled, that is, more aligned with isobaths. Note that in the mean, near-surface currents as indicated by these locations (and others, not shown) are anticyclonic, while near-bottom currents are cyclonic around the gulf (see appendix B, Fig. B1). To assess the

---

[4] Additionally, there is complication due to the existence of a forced solution (especially under the LC at station A in Fig. 13a). Another source of discrepancy is that the analytical solution is for single period while numerical profile represent response within a range of periods from 20 to 100 days.

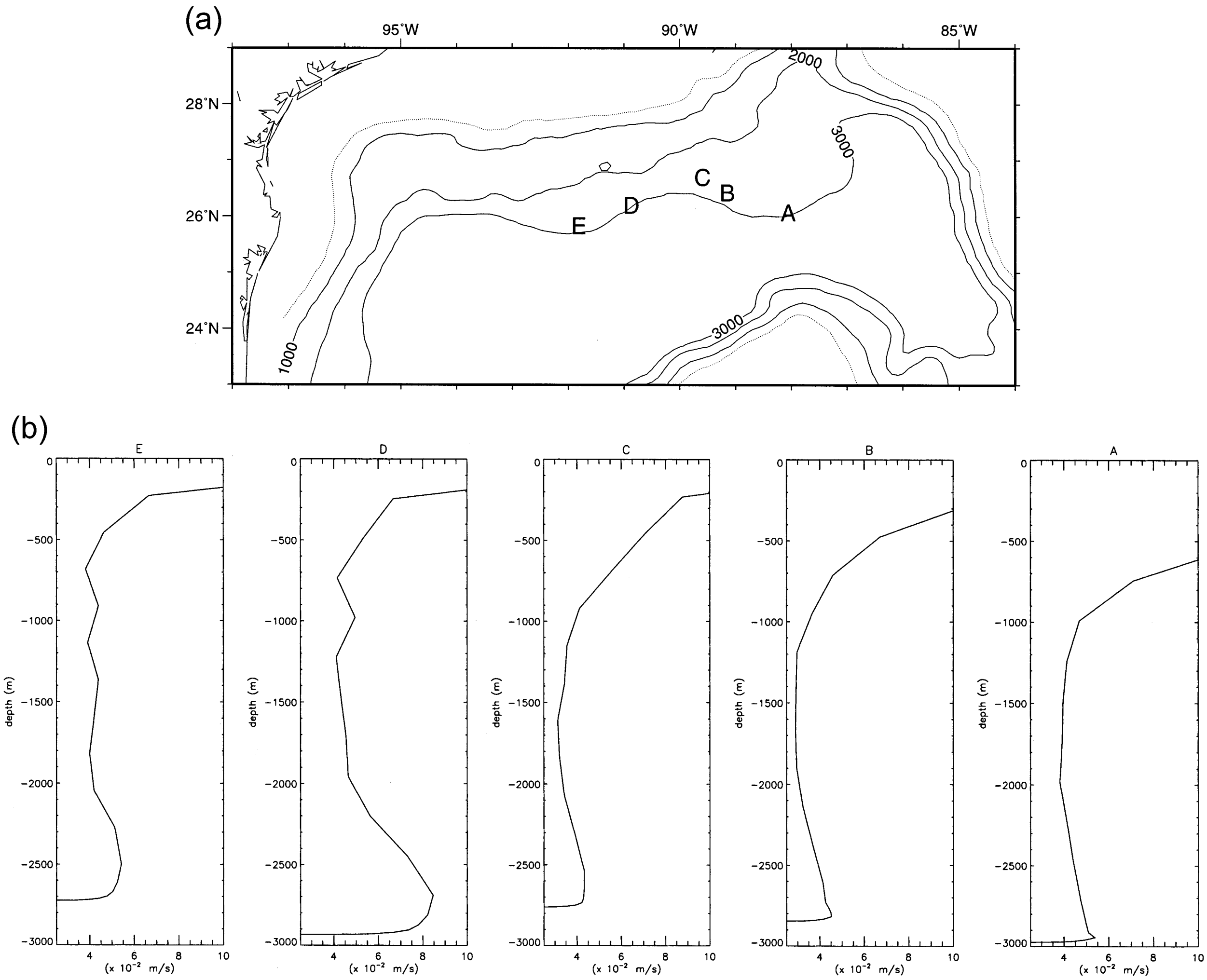

FIG. 13. (a) Five locations along ray 2 (see Fig. 11a) where vertical profiles of the square root of kinetic energy in the 20–100-day band are plotted in (b). (b) Vertical profiles of the square root of kinetic energy in the 20–100-day band at the five locations along ray 2 shown in (a).

effects of deep currents on ray properties, appendix B extends the ray equations (5b) and (6) to include the ambient mean currents of Fig. B1. One important effect is to change the velocity of the ray, (B3), which in general increases the westward propagation speed. The green curves in the lower panel of Fig. 11a show that with deep currents, rays 2 and 3 have looped around the western portion of the model gulf. The averaged group speed increases from 9 to 12 km day^{-1} (dotted curve in Fig. 11b, top-left panel). The latter value agrees with O96, who also found (from correlation and time-lag analysis) a value of 12 km day^{-1}. A less obvious effect is that current shears (and divergences) also diffract rays (Lighthill 1978; see below) as can be seen from (B6). These tend to "bend" rays into the main CGKE region especially in the western gulf, thus improving the overlapping of rays with areas of more significant LOKE$|_{20\text{–}100\mathrm{d}}$ obtained from the numerical simulation (Fig. 11a, lower panel; see also Fig. 11b where changes in ray properties of ray 2 are given).

Ray 3 originates from a location just outside the direct influence of the LC north–south pulsation, but affected by LCE sheddings and passages. Its path is similar to that of ray 2. It propagates upslope, and after crossing the 3000-m isobath, converges with ray 2 westward from approximately the 90°W. We conclude therefore that rays 1, 2, and 3 represent waves that originate from a region of active LC and LCE fluctuations. The paths traced by these rays coincide well with the eastern portion (from 86° to 92°W) of the CGKE band. East of approximately the 89°W, the band is likely a result of both locally forced (by LE and LCEs) and TRW components. West of 89°W, free TRWs are likely as the direct influence of LC and LCEs is almost nil.

Rays 4, 5, and 6 are chosen to originate from the northern rims of propagating LCEs. Ray 4 first propa-

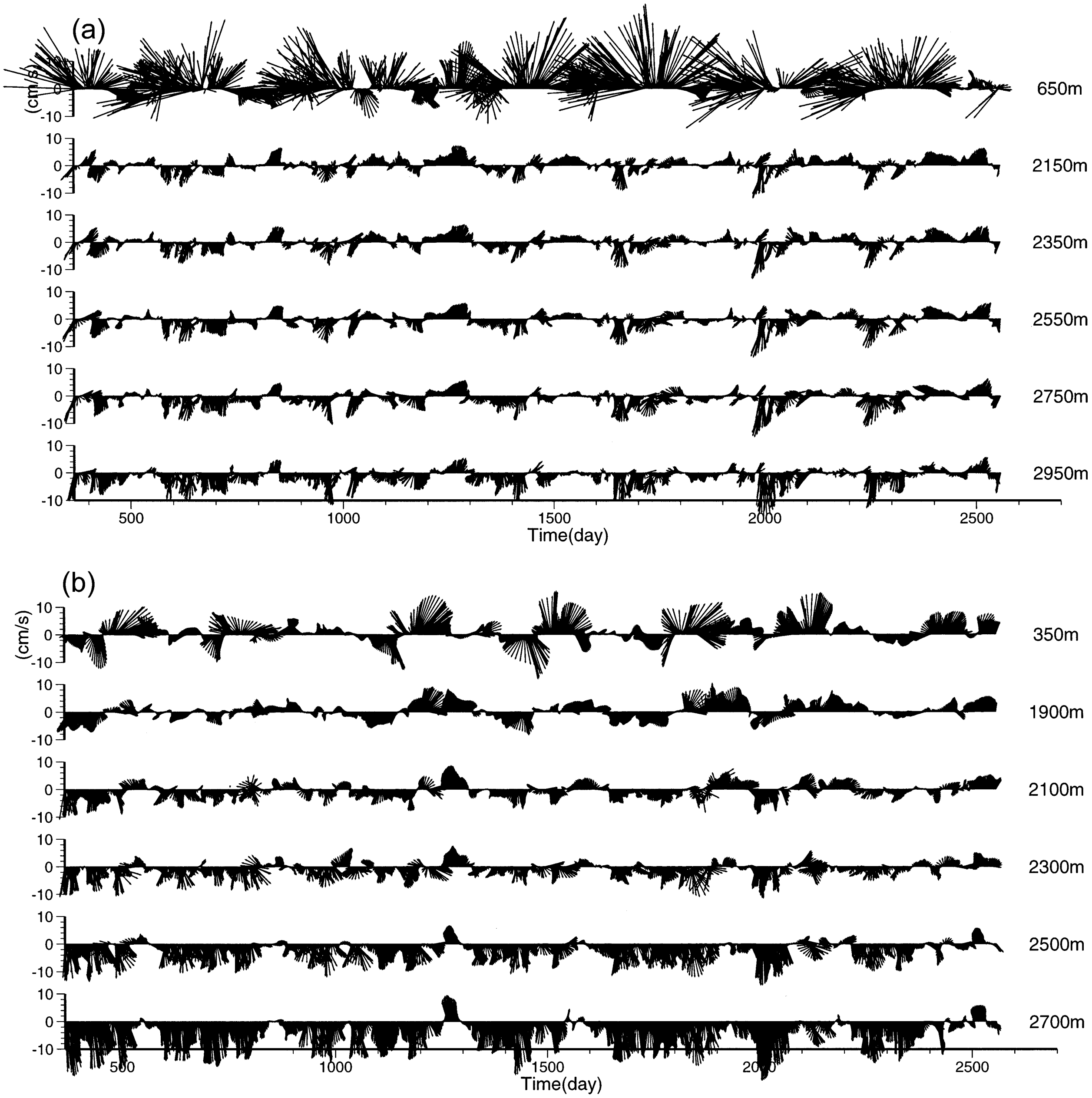

FIG. 14. (a) Vector stick plots at location A of Fig. 13a, upward from the near-bottom depth level where the LOKE$|_{20\text{–}100\text{d}}$ shows maximum. The top panel shows vectors at a representative near-surface level. In these plots y-directed sticks denote motions parallel to the local isobath, positive clockwise around the gulf (i.e., generally eastward). (b) As in (a) but for location D of Fig. 13a.

gates northwestward, turns southwestward, and then westward to remain just offshore of the 3000-m isobath before crossing it at approximately the 92°W. Being initially over a relatively gently sloping portion of the central gulf, ray 4 starts off as a predominantly planetary Rossby wave (group velocity ~ -5 km day^{-1}), and then quickly becomes TRW with its group speed increasing to $\sim$10 km day^{-1}. Rays 5, 6, and another ray further west (not shown) in part account for the moderate LOKE$|_{20\text{–}100\text{d}}$ near the western gulf ($\sim$93 to 25°N, 94.5°W). They exist as mixed topographic and planetary Rossby waves as $\beta_{\text{Topo}}/\beta$ remains below 10 through most of their paths. We also trace rays 4, 5, and 6 backward (from stations 4, 5, and 6). The results (not shown) indicate that they do not connect back to the LCE shedding zone in the eastern gulf. This confirms that the energy along these rays originates from propagating LCEs in the central gulf.

Similar to what we have discussed above for ray 2, we have also conducted for other rays the depth-profile analysis (cf. Figs. 13 and 14) that confirms the near-bottom intensification of currents, and also the wavenumber analysis (cf. Fig. 12), based on the PE model results, that confirms that the (k, l) pairs at locations on ray paths are consistent with the TRW dispersion curves. These, the phase and correlation analysis (Fig. 8), and the coincidence of ray paths with the CGKE band (Fig. 11), strongly support that TRWs exist in the PE model results. In summary, we conclude that the CGKE band can be accounted for by two types of TRWs. The first is a predominantly topographic Rossby wave type that originates under the region of active LC and LCE fluctuations in the eastern gulf and that tends to be channeled between the 2000- and 3000-m isobaths. Though the CGKE band and rays extend into the western gulf, we caution that wave-shortening due to refraction means that the waves are underresolved (~west of 92°–93°W) with the present (PE) model's resolution. The second is a mixed topographic and planetary Rossby wave type that originates from under LCEs that propagate southwestward over the deeper waters of the central gulf. These waves account for LOKE$|_{20-100\mathrm{d}}$ found offshore of the 3000-m isobath in the western gulf.

4) Effects of wavelength, stratification, periods, and deep currents on rays

We mentioned previously that the averaged TRW wavelengths deduced from the simulation results are shorter than Hamilton's (1990) estimates from observations. Hamilton reported wavelengths from 110 to 300 km, while estimates from the numerical simulation range from 63 to 210 km, and we have used an average of 110 km as the initial condition for ray-tracing. The wide range suggests that the WKB assumption of slowly varying (time and space) N (and other environmental variables) may not be strictly satisfied in the simulation results. We find also that N varies depending on the depth range used for averaging. Thus $N \approx 2.5 \times 10^{-4}\ \mathrm{s}^{-1}$ over the CGKE region if only the lowest 500 m is used. Figure 12 also plots, for each of the four periods, the dispersion curves corresponding to $N = 6.25 \times 10^{-4}\ \mathrm{s}^{-1}$ (dotted curves), an average of the benchmark $N \approx 10^{-3}\ \mathrm{s}^{-1}$ (approximately over the 3000-m isobath) and $N = 2.5 \times 10^{-4}\ \mathrm{s}^{-1}$. Thus the estimated ($k_0$, l_0) pairs are within the range of uncertainty in N. This uncertainty is also reflected in the value used by Hamilton, $N = 5 \times 10^{-4}\ \mathrm{s}^{-1}$, an averaged value based on CTD casts for 1500- to 3000-m depth in the central gulf. In view of the wide ranges in which both N and $2\pi/K$ can vary, it is of interest to examine how they affect the ray paths.

The effects of $\mathbf{K}$, N, and σ on rays can be assessed from (3) and (7) (again assuming $\beta_{\mathrm{Topo}}/\beta \gg 1$, which is a good approximation). The former shows that $|\mathbf{C}_g| = N|\nabla h|/K$, so that group speed increases with wavelength but decreases with N. The ray path also depends on the direction of $\mathbf{C}_g$, or on the requirement that σ is constant (or σ_a = constant when $\mathbf{u}_{\mathrm{deep}}$ is included; see appendix B) along the ray. For $NhK/|f| \approx 1$, the tanh term changes slowly for changes in its argument and can be assumed constant. Equation (7) shows then that for fixed N and σ, increasing the wavelength (from the 110 km used in Fig. 11a) will merely increase the group speeds of the rays, otherwise the ray paths are similar to those shown in Fig. 11a (not shown).[5] However, if N (and/or period) is decreased, the angle θ would increase and rays would tend to propagate more upslope than those shown in Fig. 11a. Though the relation is nonlinear [(5a) and (6)], we find that these deductions based on (3) and (7) provide a fairly accurate picture of the effects of changes in wavelength, stratification, and period on the ray path. In the top panel of Fig. 15, we plot two rays starting from station 2, the original ray from Fig. 11a with $N = 10^{-3}\ \mathrm{s}^{-1}$ and $2\pi/K = 110$ km, and a more upslope ray for $N = 6.25 \times 10^{-4}\ \mathrm{s}^{-1}$ and $2\pi/K = 150$ km (both rays are virtually unchanged when $2\pi/K$ is increased to, say, 250 km—when the time variable is scaled by ratio of the original K to new K to account for the corresponding increase in the group speed). Since only the ratio σ/N matters in (7), we find that for $N = 10^{-3}\ \mathrm{s}^{-1}$, rays propagate upslope for $2\pi/\sigma \approx 43$ days or shorter, similar to the upslope ray of Fig. 15. It appears therefore that the CGKE band seen in the simulation cannot be explained by shorter-period TRWs (<43 days) and/or TRWs at lower possible ranges of $N < 10^{-3}\ \mathrm{s}^{-1}$.

The situation is different when $\mathbf{u}_{\mathrm{deep}}$ is included. The generally westward flow with cyclonic shear between the 1000–2000-m and 3500-m isobaths (Fig. B1), coupled with increasing $N|\nabla h|$, constitute sufficiently strong constraints for rays to bend downslope [see (B9)].[6] The lower panel of Fig. 15 shows this effect and shows how rays are confined to remain in the vicinity of the 3000-m isobath. Extensive tests verify that this confinement of rays is valid also for rays of other periods, 32, 42.7, and 51.2 days, for longer wavelengths up to ≈250 km, and also for other stations. Figure 15 shows that the downslope turning of the ray is first affected near 90° ~ 91°W in a region of cyclonic shear ($\zeta \approx 0.05f\ \mathrm{s}^{-1}$). The amount of turning caused by current shear as ray propagates upslope can be estimated from (B9):

$$\delta\theta|_{\zeta\neq 0} \approx -\int_{\mathrm{ray}} |k|\zeta/(|\nabla h|N)C_{g2}\,dt, \qquad (9)$$

which with appropriate values (from the PE model) $|k| \approx 0.01\ \mathrm{km}^{-1}$, $\zeta \approx 0.05f\ \mathrm{s}^{-1}$, $|\nabla h|N \approx 5 \times 10^{-6}$

---

[5] We have found this insensitivity of the ray path to wavelength to be valid for $2\pi/K$ up to ~250 km.

[6] Intuitively, rays are "blown downwind" or westward. This is more so in the upper than lower slope region if a cyclonic shear exists.

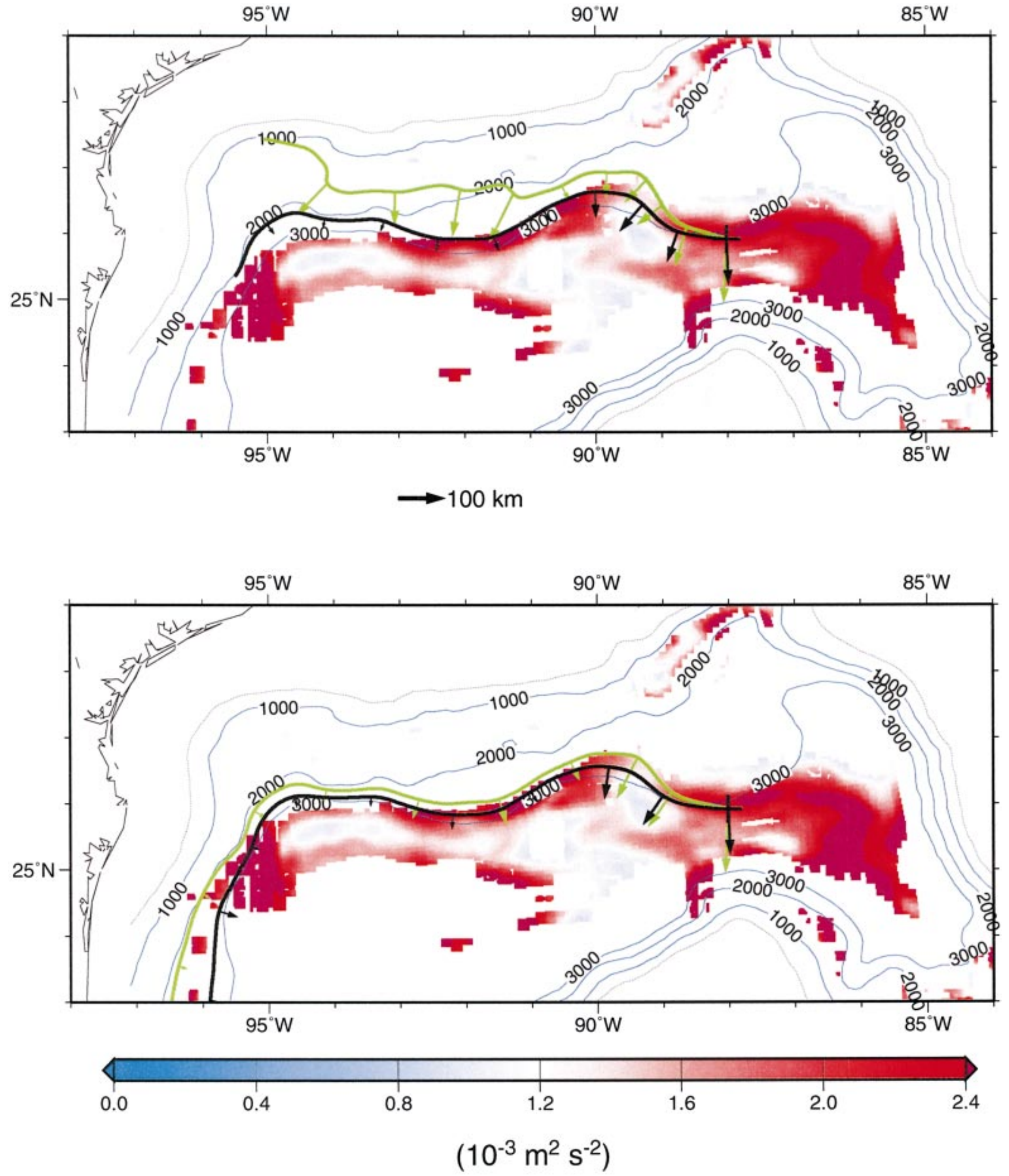

FIG. 15. Sixty-four-day-period TRW rays traced from station 2 using the benchmark N field of Fig. 10 and initial $2\pi/K = 100$ km (black ray on downslope side), and $0.625 \times$ benchmark N and initial $2\pi/K = 150$ km (green ray on upslope side). Top panel does not include $\mathbf{u}_{\text{deep}}$; lower panel does. In both panels, the LOKE$|_{20\text{–}100\text{d}}$ contours from Fig. 6 are superimposed.

s^{-1}, and $\int_{\text{ray}} C_{g2}\, dt \approx 10$ km gives $\delta\theta|_{\zeta\neq 0} \approx -4°$. This value, while reasonable, is likely to be an underestimated one. As explained in appendix B, since $d(|\nabla h|N)/dt > 0$, dk_i^2/dt also >0 [from (8) or (B7)], and the mere existence of a deep current (without shear) in the direction of k (<0) would cause rays to turn downslope, that is, contributes to additional (more negative) $\delta\theta$. An upper-bound (i.e., maximum possible turning) estimate of this latter effect is obtained from (B8) and (8) with $\zeta = 0$:

$$\delta\theta|_{\zeta=0} = \int_{\text{ray}} (d|k|/dt)(|\nabla h|N)^{-1} u_{\text{deep}}\, dt$$

$$> \int_{\text{ray}} (\partial|\nabla h|/\partial y)|\nabla h|^{-1} u_{\text{deep}}\, dt, \qquad (10)$$

which with $(\partial|\nabla h|/\partial y)|\nabla h|^{-1} \approx 2 \times 10^{-2}$ km^{-1} and $\int_{\text{ray}} u_{\text{deep}}\, dt \approx -5$ km gives $0 > \delta\theta|_{\zeta=0} > -6°$ or roughly the same contribution as that from current shear alone.

We conclude therefore that the presence of deep currents over the 2000–3500-m isobaths (Fig. B1) explains why in the PE model simulation there is little LOKE upslope, that is, why the LOKE is predominantly confined within the CGKE band. This is particularly so for TRW rays with periods shorter than about 43 days, and the ray confinement is more effective when the current also contains a cyclonic shear.

5. Discussion

The model LC executes a south–north–south vacillation approximately every 5–6 months and sheds off an LCE every 10 months or so. These periods are too long for a direct forcing of the TRWs. The vorticity maps of Fig. 3 show the appearance of small-scale disturbances around the LC and shedding and propagating LCEs. The study of these *meanders* (i.e., the mechanism of how they are produced) clearly deserves a separate treatment and is outside the scope of this paper. In the following, we merely show how these short-scale fluctuations can provide the necessary linkage for energy transfer from the LC and LCEs to deep motions. We also give an example of a specific TRW event and discuss what ray paths may mean to the existence of deep currents.

a. Sources of TRW energy

As an example, we again focus on station 2, the origin (energy source) for ray 2 (results at other stations are similar). Figure 16 shows, at 5-day interval, vorticity maps in an enlarged region of the LC during a period of its northward extrusion before an eddy-shedding event. It shows clearly the appearance of high cyclonic vorticity perturbations that propagate around the LC and into the Florida Straits (e.g., day 901–921 and also day 931–956). The source of these cyclonic disturbances appears to be along the western edge of the LC in the Yucatan Strait. The meander begins as these disturbances traverse across the Yucatan shelf and slope into the deep gulf (e.g., day 921, 926, and 931). Because of the color contrast, cyclones are most visible in these maps, but propagating anticyclones are also present. These cyclones and anticyclones constitute the propagating meanders we referred to above. By noting the recurrences of the meanders from these and other similar maps, one may infer time scales (periods) of approximately 20–60 days, and spatial scales (wavelengths) about 100–200 km. To examine more closely how these shorter-scale fluctuations near the surface excite deep currents, we performed time series analyses of various dynamical variables at several stations. An example at station 2 of Fig. 11 (shown as the + point in Fig. 16) is given in Fig. 17. The top two panels give time variations of the layer-1 depth and (relative) vorticity, respectively, that cover approximately five periods of northward LC extrusion and eddy shedding. LCE shedding occurs at approximately model day 450, 750, 1150, 1500, and 1800 (denoted by the symbol E in each panel; cf. Fig. 3b), each time at the ''foot'' of a sudden drop in layer-1 depth. The drop is followed by a trough (i.e., low) that lasts approximately 100 days, and then a relatively slower rise that crests in approximately 200 days, signifying the northward extrusion of LC past the station. On these LC-extrusion and LCE-shedding timescales, the vorticity is highly anticorrelated with layer-1 depth: it becomes more negative (i.e., anticyclonic) during layer 1's rise and maximizes to about zero vorticity during layer 1's trough. Apparent in the vorticity time series is the existence of high-frequency fluctuations during periods of LC extrusion (when ζ/f becomes more negative and layer 1 deepens), and the absence of these fluctuations when the LC retreats southward of the station after each shedding. (The layer-1 depth time series shows similar, though less transparent, characteristics.) It is clear that these fluctuations are associated with propagating meanders and other LC variability when the latter extends northward (Fig. 16).

The existence of these fluctuations in the 20–100-day TRW periods can be most clearly seen in the bandpassed time series. The middle two panels of Fig. 17 show 20–50-day bandpassed kinetic energy in layers 1 and 4, respectively, and lower two panels show same in the 50–100-day periods. The plots show clearly the amplification of these shorter period (i.e., periods less than LC north–south vacillation and LCE-shedding periods) fluctuations near the surface during the LC's northward extrusion phase, and also how they almost disappear when the LC retracts following a shedding event. The fluctuations transmit to the lower layer (4), where the energy of the combined 20–50-day and 50–100-day accounts for approximately 64% of the total lower-layer energy. Thus longer-period LC vacillations and LCE sheddings near the surface have little direct signature in the lower layer (they actually account for less than 10% of the lower-layer energy, with the remaining approximately 25% residing in the almost steady bottom currents), while the short-scale parasite fluctuations they produce, which account for only 37% of the near-surface kinetic energy (Fig. 17), have profound impact on the lower-layer motions.

To infer the interconnections between the upper and lower-layer fluctuations, we calculated time-lagged correlations of various quantities focusing in the 20–100-day periods. Let h_i, ζ_i, and KE_i be the fluctuations in the layer depth, relative vorticity and kinetic energy, respectively, of the ith layer. Typical for these time series, correlations which exceed 0.15 differ from zero at the 95% confidence level. We find then that h_1 and ζ_1 are *negatively* correlated $= -0.5$, with the former leading slightly by 1 day. Since potential vorticity is conserved, the negative correlation (and nonzero lag) suggests the importance of advection in layer 1 where currents due to the LC are strong, typically of $O(1\ \mathrm{m\ s^{-1}})$. On the contrary, h_4 and ζ_4 are positively correlated =

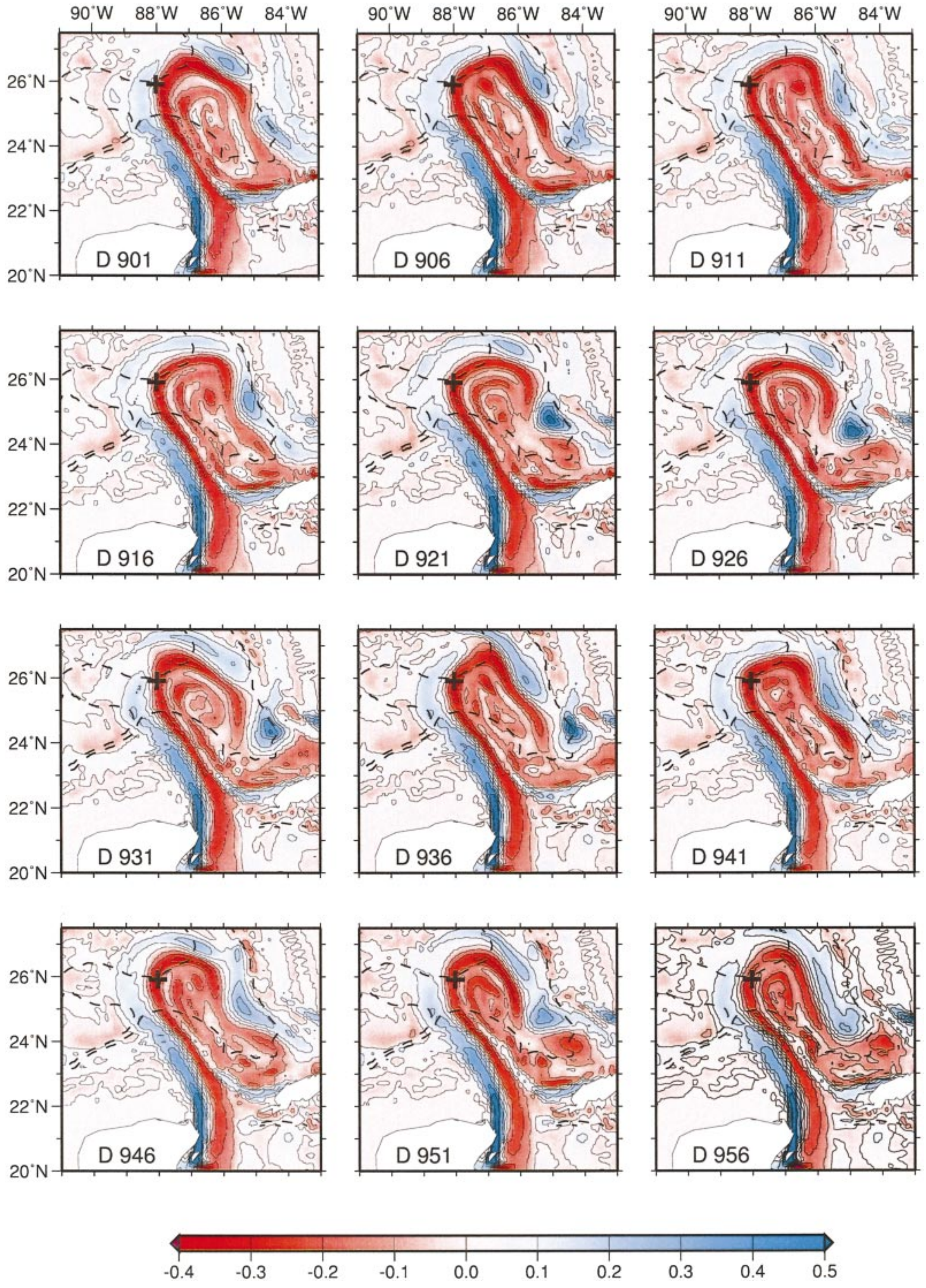

FIG. 16. Relative vorticity maps at 5-day interval in an enlarged region of the LC during a period of its northward extrusion before an eddy shedding event (on day 1150, not shown). The + symbol indicates origin of ray 2 of Fig. 11a. Dashed contours denote the 3000- and 3500-m isobaths.

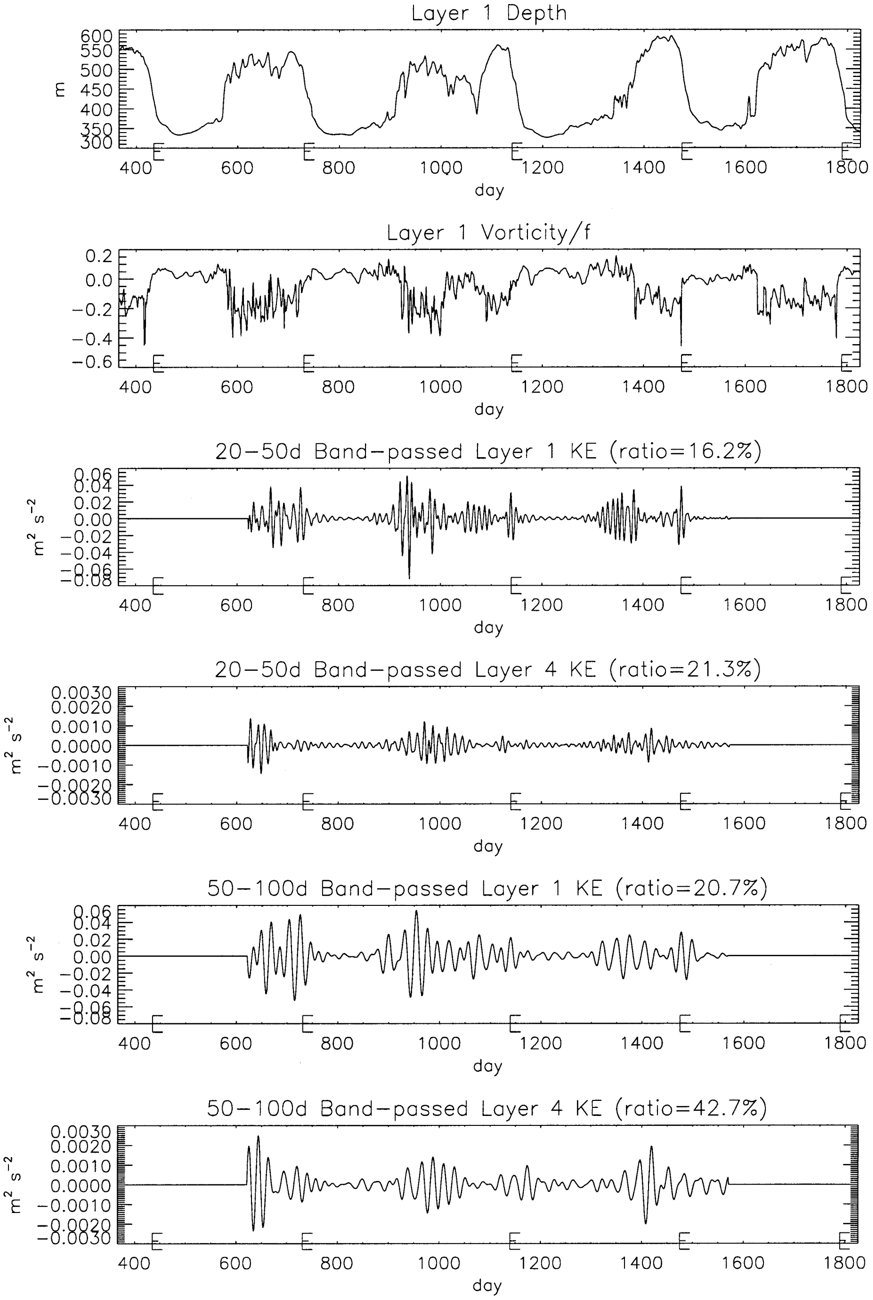

FIG. 17. Time series at station 2 (i.e., the + point in Fig. 16). (top two panels) Time variations of the layer-1 depth and (relative) vorticity; (middle two panels) 20–50-day band-passed kinetic energy in layers 1 and 4; (bottom two panels) 50–100-day band-passed kinetic energy in layers 1 and 4. The symbol E along the x axis indicates times when LCEs are shed in the PE model. Ratio (in panels 3–6) = (energy in respective band)/(energy over the entire spectrum).

0.5 with zero lag, which suggests excellent *local* conservation of potential vorticity: $\partial[(f + \zeta_4)/h_4]/\partial t \approx 0$. The link between near-surface and near-bottom motions comes through h_1 and h_4, which are negatively correlated = −0.6, with h_1 leading h_4 by about 3 days. Thus bottom energy in the 20–100-day periods originates from region under active LC and LCE variability, and its excitation by LC and LCEs therefore goes as follows. Through dynamical instability of some kind, propagating meanders develop around the perimeter of these larger-scale features, where currents are strong (~1 m s^{-1}) and strongly sheared. These meanders have length scales of $O(100 \sim 200$ km) and temporal scales of about 20–60 days (Fig. 16). Though not as readily identified from the vorticity maps, there also exist fluctuations of comparable energy in the 50–100-day band (Fig. 17). Variations that cause layer stretching (shrinking) near the surface force shrinking (stretching) of the near-bottom layer, which through potential vorticity conservation induces anticyclonic (cyclonic) near-bottom vorticity. It is not entirely trivial however, how these near-bottom vorticity fluctuations translate into the kinetic energy of TRWs (included in KE_4). Indeed, we have not studied the conditions under which a transfer of energy from the surface meanders to TRW motions can be possible. The transfer *may be* caused by the phase-matching mechanism proposed by Pickart (1995; due originally to Malanotte-Rizzoli; see also Pedlosky 1977), especially in the vicinity of station 2 where the 3000-m isobath tilts from southwest to northeast (Fig. 16; similarly also for station 1 on the 3200-m isobath). This tilt allows eastward TRW phase propagation (Fig. 1) that can couple with the eastward meanders that propagate past this station, so that energy radiation becomes possible. In Pickart's case, this coupling mechanism explains that the TRW energy he found off Cape Hatteras was forced by eastward Gulf Stream meanders. A similar mechanism may be at work also in the present PE model simulation (see below), though clearly this needs to be studied in more detail, preferably within a more idealized model setting.

Though weaker in strengths, similar excitations of TRWs by meanders around the LC as described above also exist around detached LCEs which propagate southwestward in the PE model (not shown). In this case, the combined planetary beta and (gentler) sloping topography in the deeper portion of the central gulf (beyond the 3000-m isobath) contribute to the west-northwestward spread of TRW energy, as discussed previously for rays 4–6 in Fig. 11a.

b. Robustness of the calculation and example of a specific event

The excitation mechanism suggested herein is apparently more akin to Pickart (1995) than to that described in Hogg (1981) and Louis et al. (1982). These latter works suggest forcing of the TRWs through response to specific ring shedding event, that is, being more of an impulse response, rather than a near-periodic forcing problem by propagating meanders. In the Gulf of Mexico, Hamilton (1990) found correlations between pairs of eastern and western moorings that were related to LCE-shedding events. On the other hand, secondary small-scale features such as meanders owe their existence to forcing by LC and LCEs, the movement of which over a specific area (topographic slope in particular) can therefore be considered as ''impulsive'' (∼1–2 weeks). While costs and logistics generally dictate that observations (of TRWs) are for specific events, modelers can afford longer-term (model) data and are compelled to demonstrate the occurrence of more than one or two specific events only, as these can arise from specialized forcing, initial and boundary conditions, and sometimes even the particular model grid being used. We have therefore resorted to an analysis of the deep EKE as a 7-yr ensemble of specific excitation and propagation events of TRWs (Figs. 6 and 11). The existence of a band of deep EKE across the central gulf (the CGKE) provides some evidence that the simulated events are robust model features that are repeatable (this is clear from animation of LOKE). To further ascertain this, we have repeated the 10-yr simulation by doubling the horizontal grid resolution. We find that this doubled-resolution experiment also gives a very similar (last 7 yr) composite map of deep EKE containing the CGKE band as in Fig. 6, and which also is made up of individual TRW excitation and propagation events. The difference is that the deep EKE is now more intense (Oey 1998). To complete the paper, we give here an example of a typical TRW excitation and propagation event taken from the doubled-resolution 7-yr ensemble. Figure 18 plots images of EKE at 188 m above the bottom[7] [model sigma-level 17; green–red–yellow, values less than 1.4×10^{-2} $(\mathrm{m\ s^{-1}})^2$ are omitted] superimposed on 200-m Eulerian trajectories (tracked for 5 days and launched at every 12th grid point) that are colored with local values of ζ/f (dark blue for cyclone ≥ 0.4 and red for anticyclone ≤ -0.4). These trajectories indicate locations of near-surface LC and eddies. For example, the LC front is delineated by the transition from red to blue trajectories. On day 1345 and 1370, the front passes over point 1 and point 2, respectively.[8] On day 1370, high EKE region is seen stretching westward and onshore from point 1, following approximately the 3000-m isobath. High EKE is also seen at point 2. On days 1385 and 1405, the high EKE progressed westward to point R, the ray-convergence zone discussed previously in conjunction with Fig. 11. Despite the rich (surface) eddy structures west of 88°W, deep EKE rarely rises above the 1.4×10^{-2} $(\mathrm{m\ s^{-1}})^2$ cutoff except near the 3000-m isobath when the high EKE arrives, a phenomenon strongly suggestive of TRW propagation as discussed previously. Figure 18 also shows two TRW rays launched from point 1 using properties at day 1345 as initial conditions, and also from point 2 using day 1370 as initial conditions; both calculations also include deep mean (7 yr) currents (see previous section). Despite the many simplifications inherent in the TRW theory, the rays are seen

---

[7] Here the EKE is dominated by energy in the 20–100 days, and contours of $\mathrm{EKE}|_{20\text{–}100\mathrm{d}}$ are virtually identical.

[8] Point 1 is the same as station 1 of Fig. 11, and point 2 is slightly south (by 0.3°, lat) of station 2. Note also that meanders typically have cross-frontal amplitude of about 50 km (i.e., ≈10 grids), and therefore cannot be readily distinguished in trajectories launched every 12 point. They are nonetheless easily seen in maps of relative vorticity as in Fig. 16.

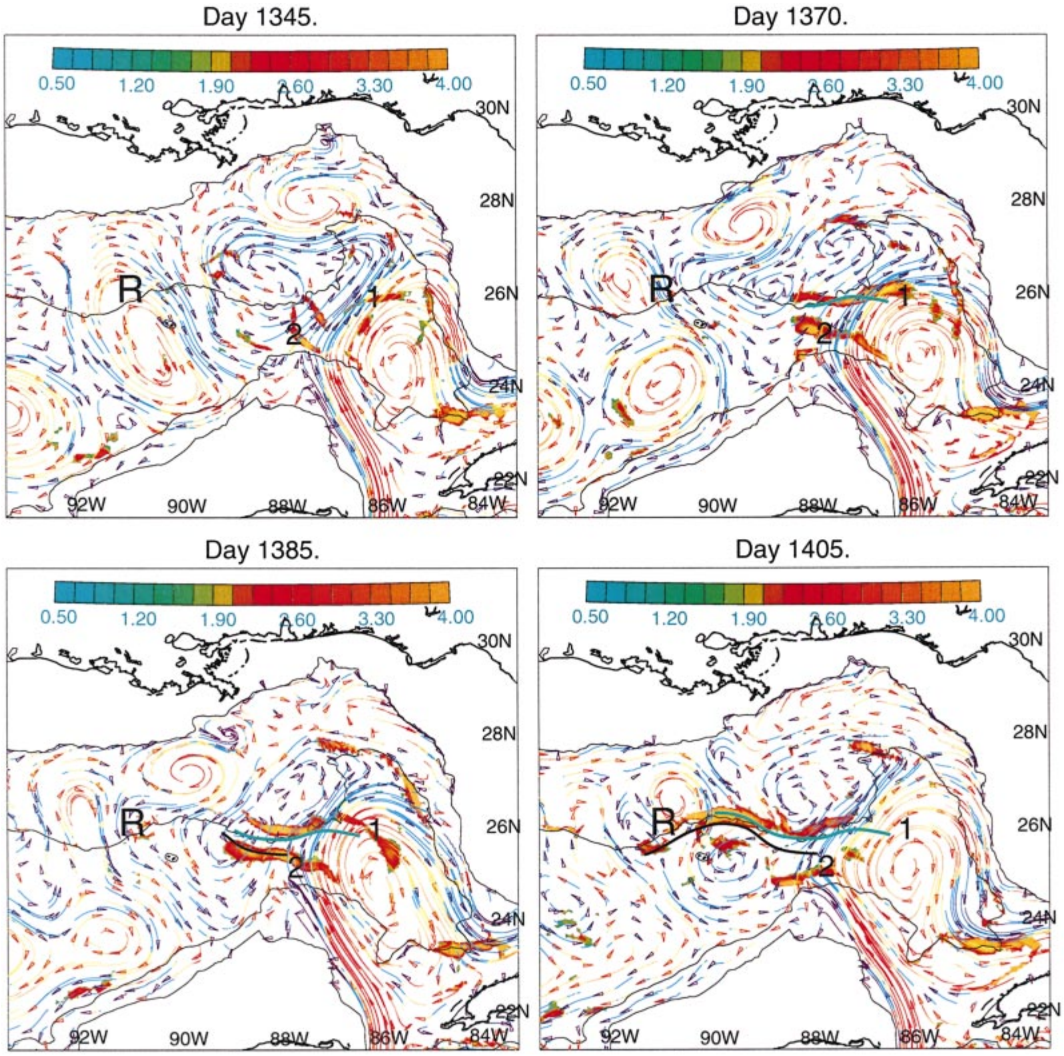
Day 1345. Day 1370. Day 1385. Day 1405.

FIG. 18. Modeled eddy kinetic energy [green-red shade, values ≤ 1.4 × 10^{-2} (m s^{-1})^2 are omitted] at 188 m above the bottom on (top left) day 1345 when the northern edge of LC touches point 1 and a TRW ray (green) is initiated there; (top right) on day 1370 when the northwestern edge of LC touches point 2 and a second TRW ray is initiated there (black); (bottom left) on day 1385; and (bottom right) day 1405. The arrowed curves are Eulerian trajectories at 200 m below the surface, released at every 12th model point and each tracked for 5 days [scale = 0.5 m s^{-1} (100 km)$^{-1}$], and colors on them indicate local values of ζ/f, dark-blue is cyclonic ≥0.4, and red is anticyclonic ≤−0.4. Solid curves are the 200-m and 3000-m isobaths. Point R marks the location where TRW rays converge. Note that despite rich (surface) eddy structures west of 88°W, deep EKE rarely rises above the 1.4 × 10^{-2} (m s^{-1})^2 cutoff except near the 3000-m isobath where TRWs pass.

to track the high EKE progression fairly well. In particular, both rays would eventually converge near 90°–91°W. Also, the velocity of progression of the EKE feature, ≈−8.3 km day^{-1}, matches well the average of the group velocities of the two rays (≈9 km day^{-1}). Similar events of excitation and propagation of TRWs are also found to be triggered by southwestward propagating LCEs in the western gulf (not shown).

c. Ray paths and the existence of deep currents

We showed that the generally westward deep currents in the model gulf increase the TRW group speeds and also confine rays to the vicinity of the 3000-m isobath in more accordance with the simulated CGKE band (Figs. 11 and 15). Thus knowledge of group speeds and ray paths may provide information on deep currents. Based on a time-lagged correlation analysis between two deep moorings, one in the eastern [mooring G at (25°36′N, 85°30′W) on 3200 m] and another one in the western [mooring Q at (25°52′N, 94°53′W) on 3000 m] gulf, Hamilton (1990) obtained a lag time of 106 days, and estimated a *lower-bound* group velocity of −9 km day^{-1} by assuming a straight-line distance between the two moorings. *If* as suggested by our ray calculation the ray path is curved approximately following the

3000-m isobath, the additional distance of 140 km would yield a group velocity of about -10.3 km day^{-1}. Hamilton also used the dispersion relation to arrive at an estimate of $|\mathbf{C}_g| \approx 8.5$ km day^{-1} based on a wavelength value of about 189 km.[9] Thus there is a difference in group velocity of about -2 km day^{-1}. Hamilton's $\mathbf{C}_g$ values can be compared with the present averaged values (after applying a small 5.5% adjustment to account for the differences in wavelength and N between Hamilton's and ours) of -11.3 and -8.5 km day^{-1}, with and without $\mathbf{u}_{\rm deep}$, respectively. In the present case, the difference, about -3 km day^{-1}, is entirely caused by $\mathbf{u}_{\rm deep}$. The -2 km day^{-1} (≈ -2 cm s^{-1}) difference in Hamilton's case may also be due to the existence of deep currents. His analysis also suggests that the observed TRWs do not stray far upslope, which may also imply existence of deep shear flows.

6. Conclusions

We would ultimately like to understand the mechanism(s) by which bottom-trapped topographic Rossby waves over the continental slope and rise of the Gulf of Mexico are generated by Loop Current and Loop Current eddy variability. Our immediate goal is more modest, however. We report here our attempt in finding evidence for TRWs from a primitive equation circulation model of the Gulf of Mexico, and in locating their possible energy sources. A 10-yr model simulation forced only by constant transport from the Atlantic was conducted so that regular LCE sheddings occur. Deep-layer analyses were then performed to band-pass motions with 20–100-day periods, a range that corresponds to that found for the observed deep EKE at the few available current-meter locations in the gulf. We found that in certain well-defined regions, over the 3000-m isobath across the central gulf in particular, spectral peaks occur within these periods; the band-passed EKE is significant (i.e., exceeds a gulf-wide standard deviation of 10^{-3} m^2 s^{-2}), exhibits bottom intensification, and accounts for over 60% of the deep energy (Fig. 6). These deep motions, moreover, occur in regions where TRWs can be supported, and the phase and correlation analysis suggests offshore and downslope phase propagation consistent with the TRW dispersion relation (Figs. 8 and 1). The wavenumber vectors computed from the PE model results are consistent with the dispersion relation (Fig. 12), and yield wavelengths of 63–210 km. These model-derived wavelengths are shorter than Hamilton's (1990) estimates of 110–300 km based on the observations. A possible source of discrepancy is due to the uncertainty in the Brunt–Väisälä frequency. By utilizing the TRW dispersion relation to track energy pathways (ray tracing), we find that the rays coincide with the above region of significant EKE over the 3000-m isobath (Fig. 11a). East of 91°W, the source of EKE comes from the LC and LCE-shedding region, while over the western gulf additional source is from the southwestward propagating LCEs. Since, in a topographically dominated region, ray directions depend primarily on the angles between wavenumber components, the computed ray paths are relatively insensitive to wavelengths, so that the (PE) modeled region of significant EKE survives despite the discrepancy between modeled and observed wavelengths. The vertical trapping scales (of the 20–100-day bottom motions) are estimated to decrease (from $\approx$600 to 300 m) with distance to the west. While exact values differ, the trend agrees with the ray solution (Fig. 11b). These rays indicate that refractions by topographic gradients and by deep currents with cyclonic shearing play an important role in confining the possible energy paths just inshore of the 3000-m isobath in the central gulf. In regions where rays are focused, the *simulated* EKEs increase (Fig. 11a at 91°, 94°, and 95°W). Refraction causes wave shortening, which suggests dissipation as TRWs propagate westward (Hamilton 1990). The presence of deep (westward) currents increases the TRW group speeds, by 2–3 km day^{-1}. This and the constraints on allowable ray path imposed by current shear may be used to infer deep currents in the gulf. The ray calculations also suggest that energy sources for the TRWs found in the PE model are from short-scale propagating meanders ($\sim$100–200-km wavelengths and $<$100-day periods) around the LC and LCEs.

A number of issues remain. First, while we have identified that the 20–100-day and O(100 km) deep motions are forced by near-surface fluctuations of similar spatial and temporal scales, we have not understood the conditions under which energy transfer can occur. Our results suggest that TRWs may play an important role in this transfer, but clearly this needs to be further investigated in a future study. Second, though we have shown their existence (in the PE model), how the near-surface, short-scale fluctuations are produced remains a research issue yet to be examined. Third, apart from the central gulf region over the 3000-m isobath, other regions in the gulf (Florida shelf/slope, deSoto Canyon, gulf southwestern slope, and Yucatan slope) are also potential sites of TRWs but were excluded by the strong constraints we somewhat arbitrarily have imposed when identifying TRWs from the simulation. The exclusion is justified since we do not believe that the present (PE) model's resolution is sufficiently refined in these steep-slope regions for a meaningful interpretation of the results. Higher-resolution model results, together with observations, should therefore be analyzed to pursue TRW research in these regions. Last, the very low frequency deep motions (periods longer than 100 days) are important and should also be studied in the future.

---

[9] Hamilton did not explicitly quote this value, but it is consistent with the averaged wavelength estimated from six of the seven values in his Table 2 (omitting the shortest-wavelength value of 110 km).

Acknowledgments. We benefited from discussions with Peter Hamilton and Bill Schmitz. Comments from both reviewers greatly improved the manuscript. We are grateful to supports from the Minerals Management Service Deep Water Modeling Program. Thanks are due to Alexis Lugo-Fernandez, the program manager, for encouragement during the course of the project. LYO also acknowledges support from the NAVO/NGLI Program through ONR. Computations were conducted at NOAA/GFDL, Princeton.

APPENDIX A

Ageostrophic Effects on TRW Dispersion Relation

Including the time-dependent terms $(u, v)_t$ and friction $-r(u, v)$, where r is a friction coefficient, the dispersion relation (assuming a QG bottom condition equation) has the same form as (1) except that μ (hence σ) is complex:

$$\mu = \pm(\mu_R + i\mu_I), \tag{A1}$$

$$(\mu_R, \mu_I) = \mathrm{NKE}^{1/2}/(f^2 - \sigma^2)^{1/2}[\cos(\chi/2), \sin(\chi/2)], \tag{A2a}$$

$$E = (A^2 + B^2)^{1/2}, \qquad \chi = \tan^{-1}(B/A),$$

$$A = 1 + k\beta/(\sigma K^2), \quad \text{and} \quad B = r/\sigma. \tag{A2b}$$

For convenience only, the above equations are written in a form that assumes that σ is real. Since ageostrophic contribution is expected to be significant only at short periods of about 10 days and less, we will set $\beta = 0$ in the following. Consider now two cases. In the first, set $r = 0$, so μ is real and is given by

$$\mu = NK/(f^2 - \sigma^2)^{1/2}. \tag{A3}$$

For simplicity, set $h_x = 0$; then the dispersion relation for $\tanh(NhK/|f|) \approx 1$ is

$$\sigma/f = (Nh_y/f)(k/K)/\{1 + [(Nh_y/f)(k/K)]^2\}^{1/2} \tag{A4}$$

and is shown as solid curves in Fig. A1. The corresponding QG relation, valid for small $(Nh_y/f)(k/K)$, is shown as dotted curves. The ageostrophic correction is distinguishable only for strong topographic slope ($Nh_y/f < -0.5$, or $|h_y| \approx 0.05$ for $N/f \approx 10$) at periods $\approx$ 10 days and shorter. In the second case, for nonzero r, μ is complex $\approx NK/(f^2 - \sigma_R^2)^{1/2}\,[1, r/(2\sigma_R)]$, where σ_R is the real part of σ. The substitution $\sigma \approx \sigma_R$ in (A2) is good when $r/|\sigma|$ is small. It can now be shown that the imaginary part of $\sigma = \sigma_I \propto -r/(2\sigma_R) < 0$. As can be anticipated, friction acts as damping.

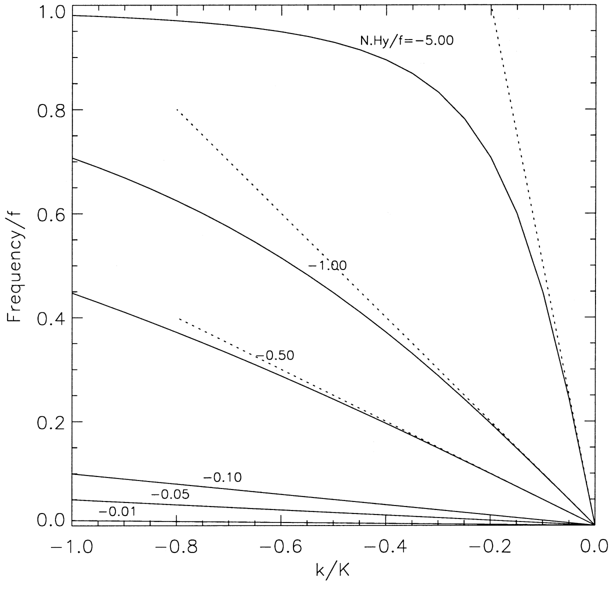

FIG. A1. Topographic Rossby wave dispersion curves (σ/f vs k/K) for (solid lines) varying topographic gradients (Nh_y/f) for the case in which the horizontal velocity field is *not* assumed to be nondivergent but the near-bottom vertical motions are still assumed to be produced by the interaction of *geostrophic* currents with bottom slope. The isobaths are assumed to be parallel to the x axis, and water depth h decreases with y. The dotted lines are the corresponding dispersion relations based on the QG theory. Note that $k/K = 0$ corresponds to $\theta = 0$ and $k/K = -1$ to $\theta = \pi/2$, where θ is the clockwise angle from the direction of steepest topographic descent, which in this case coincides with the *negative y* axis.

APPENDIX B

The Ray Equations that Include Effects of Deep Mean Flow

Figure B1 shows the (PE) modeled currents averaged over the last 7 yr of the 10-yr simulation, at 200 m above the bottom in the gulf (L.-Y. Oey et al. 2002, unpublished manuscript). Shaded portions correspond to the $\mathrm{LOKE}|_{20\text{–}100\mathrm{d}}$ regions of Fig. 6. The modeled deep mean flow, $\mathbf{u}_{\mathrm{deep}} = (u_1, u_2)$, is generally cyclonic around the deep gulf. In the $\mathrm{LOKE}|_{20\text{–}100\mathrm{d}}$ region, maximum speed reaches 0.07 m s^{-1}, but in general it is more sluggish, at 0.03 m s^{-1}. Given TRW group speeds of about 10 km day^{-1}, the effects of $\mathbf{u}_{\mathrm{deep}}$ can be as much as 50% or more at some location. To assess the effects, the ray equations of section 2 are modified to account for $\mathbf{u}_{\mathrm{deep}}$ as follows (Lighthill 1978). First, the absolute frequency σ_a is connected to the relative frequency σ (i.e., relative to medium at rest) of section 2 by the Doppler relation:

$$\sigma_a = \sigma + u_j k_j. \tag{B1}$$

Thus the group velocity $\mathbf{C}_{ga}$ becomes

$$C_{gai} = \partial\sigma_a/\partial k_i = \partial\sigma/\partial k_i + u_i = C_{gi} + u_i, \tag{B2}$$

where C_{gi} is defined as in section 2 by (3). Thus the ray path is defined by

$$dx_i/dt = C_{gi} + u_i. \tag{B3}$$

The phase equation [(4)] is unchanged provided that σ_a from (B1) is used in place of σ:

$$\partial\alpha/\partial x_i = -k_i, \qquad \partial\alpha/\partial t = \sigma + u_j k_j. \tag{B4}$$

Thus, as in the derivation of (5a), we differentiate the

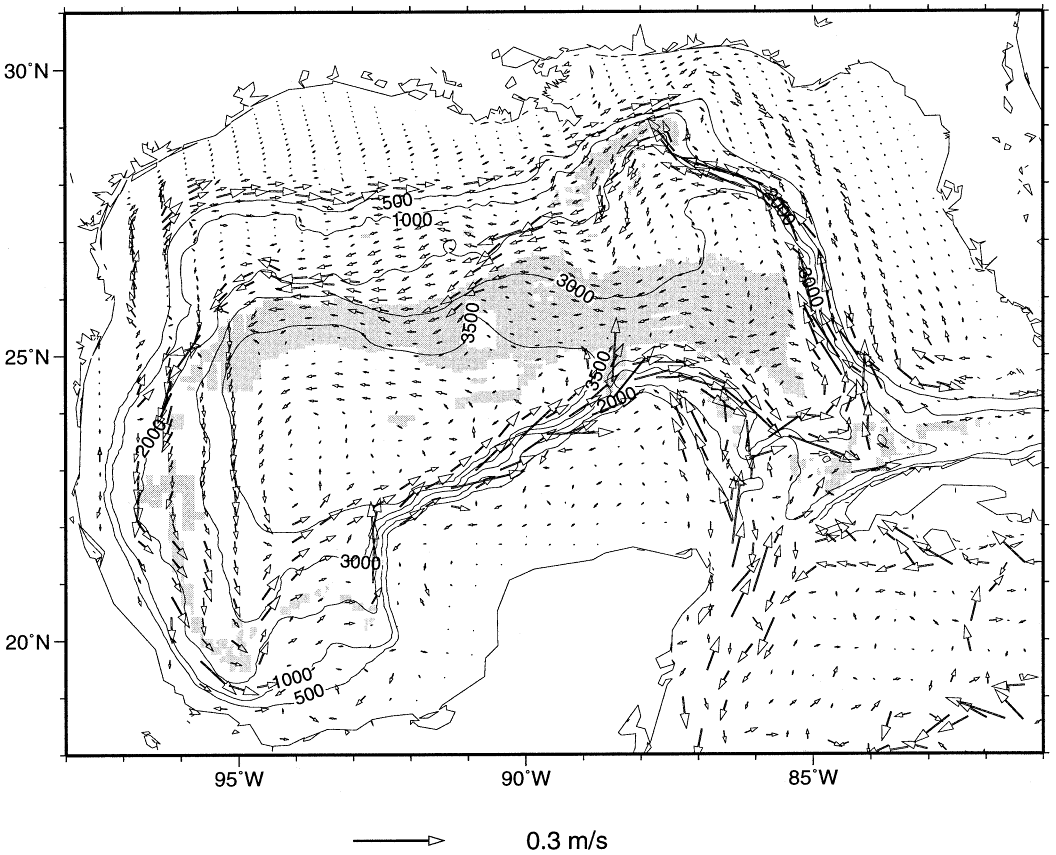

FIG. B1. The modeled currents averaged over the last 7 yr of the 10-yr simulation, at 200 m above the bottom in the gulf, from L.-Y. Oey et al. (2002, unpublished manuscript). Shaded portions correspond to the LOKE$|_{20\text{–}100\text{d}}$ region of Fig. 6.

second of (B4) with respect to x_i and make use of the first and also of (B3) to obtain

$$\partial k_i/\partial t + C_{gaj}(\partial k_i/\partial x_j) = -(\partial \sigma/\partial E_n)(\partial E_n/\partial x_i) - k_j(\partial u_j/\partial x_i), \quad \text{or} \tag{B5}$$

$$dk_i/dt = -\partial\sigma/\partial x_i - k_j(\partial u_j/\partial x_i). \tag{B6}$$

Equations (B6) and (B3) are used [in place of (5b) and (6)] to trace rays when effects of mean flow are to be included. One can multiply (B6) by k_i and assume zonal h and N (or locally functions of the diabatic coordinate y) as in (8), and also $\mathbf{u}_{\text{deep}} = [u_{\text{deep}}(y), 0]$, we obtain an estimate of how wavelength changes along rays embedded in a mean sheared flow:[B1]

$$d(k_i^2/2)/dt = -l\sin(\theta)\partial(|h_y|N)/\partial y - kl(\partial u_{\text{deep}}/\partial y). \tag{B7}$$

This shows that the effect of u_{deep} is that, for positive kl, wave shortens as the ray propagates into a region of cyclonic sheared current $\partial u_{\text{deep}}/\partial y < 0$.

Using (B1), (B3), and (B5), one readily shows that $d\sigma_a/dt = 0$ along a ray. It follows then from (B1) that $\sigma + u_i k_i$ is constant on a ray. Assuming again a zonal shear flow and using (7), we can estimate how rays are bent (i.e., how θ changes along rays) by the sheared current:

$$N|\nabla h|\sin(\theta) = -u_{\text{deep}}(y)k. \tag{B8}$$

Since $k < 0$,

$$d[N|\nabla h|\sin(\theta)]/dt = d(|k|u_{\text{deep}})/dt < 0 \tag{B9}$$

for rays propagating upslope into a region of decreasing parabathic current (i.e., cyclonic shear). Thus the effect of cyclonic shear alone is to bend rays back toward downslope (i.e., θ decreases). Note that if furthermore $N|\nabla h|$ increases upslope, then $d(k_i^2/2)/dt > 0$ from (8) and it is only necessary that $u_{\text{deep}} < 0$ for it to have the effect of bending rays downslope.

Note that the above tacitly assumes $|\partial \mathbf{u}_{\text{deep}}/\partial z| \ll 1$, that is, small vertical shears. This is consistent with a slowly varying N (over TRW wavelengths and periods) required by the use of the theory of bottom-trapped TRW; that is, the dispersion relation in (1) and Lighthill's (1978) slowly varying, z-independent phase function α. The results presented in this work

---

[B1] Again, as in (7), within the WKB framework, one can use a natural coordinate such that positive y points in the direction *opposite* to the vector ∇h, so that the argument is locally valid.

(e.g., Fig. 11b) suggest that in comparison with topographic vorticity gradient, gradients in N play a relatively minor role. While the theory is self-consistent in this regard, the question as to how a non-slowly varying N will affect ray paths, including the possible energy coupling of near-bottom with layers above, is beyond the scope of this paper.

REFERENCES

Forristal, G. Z., K. J. Schaudt, and C. K. Cooper, 1992: Evolution and kinematics of a Loop Current eddy in the Gulf of Mexico during 1985. *J. Geophys. Res.,* **97,** 2173–2184.

Gill, A. E., 1982: *Atmosphere–Ocean Dynamics.* Academic Press, 662 pp.

Hamilton, P., 1990: Deep currents in the Gulf of Mexico. *J. Phys. Oceanogr.,* **20,** 1087–1104.

——, 1992: Lower continental slope cyclonic eddies in the central Gulf of Mexico. *J. Geophys. Res.,* **97,** 2185–2200.

——, G. S. Fargion, and D. C. Biggs, 1999: Loop Current eddy paths in the western Gulf of Mexico. *J. Phys. Oceanogr.,* **29,** 1180–1207.

Haney, R. L., 1991: On the pressure gradient force over steep topography in sigma coordinate ocean models. *J. Phys. Oceanogr.,* **21,** 610–619.

Hogg, N. G., 1981: Topographic waves along 70°W on the continental rise. *J. Mar. Res.,* **39,** 627–649.

Hurlburt, H. E., and J. D. Thompson, 1980: A numerical study of Loop Current intrusions and eddy shedding. *J. Phys. Oceanogr.,* **10,** 1611–1651.

Johns, W. E., and D. R. Watts, 1986: Time scales and structure of topographic Rossby waves and meanders in the deep Gulf Stream. *J. Mar. Res.,* **44,** 267–290.

Kirwan, A. D., Jr., J. K. Lewis, A. W. Indest, P. Reinersman, and I. Quintero, 1988: Observed and simulated kinematic properties of Loop Current rings. *J. Geophys. Res.,* **93,** 1189–1198.

Levitus, S., and R. I. Gelfeld, 1992: NODC inventory of physical oceanographic profiles. Key to Oceanographic Records Doc. 18, NODC, 36 pp.

Lighthill, M. J., 1978: *Waves in Fluids.* Cambridge University Press, 520 pp.

Louis, J. P., B. D. Petrie, and P. C. Smith, 1982: Observations of topographic Rossby waves on the continental margin off Nova Scotia. *J. Phys. Oceanogr.,* **12,** 47–55.

Mellor, G. L., 1993: Princeton Ocean Model user's guide. [Available online at http://www.aos.princeton.edu/WWWPUBLIC/htdocs.pom.]

——, T. Ezer, and L.-Y. Oey, 1994: The pressure gradient conundrum of sigma coordinate ocean models. *J. Atmos. Oceanic Technol.,* **11,** 1126–1134.

——, L.-Y. Oey, and T. Ezer, 1998: Sigma coordinate pressure gradient errors and the seamount problem. *J. Atmos. Oceanic Technol.,* **15,** 1122–1131.

Oey, L.-Y., 1996: Simulation of mesoscale variability in the Gulf of Mexico. *J. Phys. Oceanogr.,* **26,** 145–175.

——, 1998: Eddy energetics in the Faroe–Shetland Channel. *Cont. Shelf Res.,* **17,** 1929–1944.

——, and P. Chen, 1992: A model simulation of circulation in the northeast Atlantic shelves and seas. *J. Geophys. Res.,* **97C,** 20 087–20 115.

——, D.-P. Wang, T. Hayward, C. Winant, and M. Hendershott, 2001: Upwelling and cyclonic regimes of the near-surface circulation in the Santa Barbara Channel. *J. Geophys. Res.,* **106C,** 9213–9222.

Paluszkiewicz, T., L. P. Atkinson, E. S. Posmentier, and C. R. McClain, 1983: Observations of a loop current frontal eddy intrusion onto the west Florida shelf. *J. Geophys. Res.,* **88** (C14), 9639–9651.

Pedlosky, J., 1977: On the radiation of meso-scale energy in the mid-ocean. *Deep-Sea Res.,* **24,** 591–600.

——, 1979: *Geophysical Fluid Dynamics.* Springer-Verlag, 624 pp.

Pickart, R. S., 1995: Gulf Stream-generated topographic Rossby waves. *J. Phys. Oceanogr.,* **25,** 574–584.

——, and D. R. Watts, 1990: Deep western boundary current variability at Cape Hatteras. *J. Mar. Res.,* **48,** 765–791.

Press, W. H., S. A. Teukolsky, W. T. Vetterling, and B. P. Flannery, 1992: *Numerical Recipes.* 2d ed. Cambridge University Press, 963 pp.

Schmitz, W. J., Jr., 1996: On the World Ocean circulation: Vol. I, Some global features/North Atlantic circulation. WHOI Tech. Rep. WHOI-96-03, 141 pp.

Smagorinsky, J., 1963: General circulation experiments with the primitive equations. Part I: The basic experiment. *Mon. Wea. Rev.,* **91,** 99–164.

Sturges, W., J. C. Evans, S. Welsh, and W. Holland, 1993: Separation of warm core rings in the Gulf of Mexico. *J. Phys. Oceanogr.,* **23,** 250–268.

Thompson, R. O. R. Y., and J. R. Luyten, 1976: Evidence for bottom-trapped topographic Rossby waves from single moorings. *Deep-Sea Res.,* **23,** 629–635.

Vukovich, F. M., B. W. Crissman, M. Bushnell, and W. J. King, 1979: Some aspects of the oceanography of the Gulf of Mexico using satellite and in-situ data. *J. Geophys. Res.,* **84,** 7749–7768.